

Does entanglement enhance single-molecule pulsed biphoton spectroscopy?

Aiman Khan,^{1,*} Francesco Albarelli,^{2,3} and Animesh Datta^{1,†}

¹*Department of Physics, University of Warwick, Coventry, CV4 7AL, United Kingdom*

²*Dipartimento di Fisica “Aldo Pontremoli”, Università degli Studi di Milano, via Celoria 16, 20133 Milan, Italy*

³*Istituto Nazionale di Fisica Nucleare, Sezione di Milano, via Celoria 16, 20133 Milan, Italy*

(Dated: July 6, 2023)

It depends. For a single molecule interacting with one mode of a biphoton probe, we show that the spectroscopic information has three contributions, only one of which is a genuine two-photon contribution. When all the scattered light can be measured, solely this contribution exists and can be fully extracted using unentangled measurements. Furthermore, this two-photon contribution can, in principle, be matched by an optimised but unentangled single-photon probe. When the matter system spontaneously emits into inaccessible modes, an advantage due to entanglement can not be ruled out. In practice, time-frequency entanglement does enhance spectroscopic performance of the oft-studied weakly-pumped spontaneous parametric down conversion (PDC) probes. For two-level systems and coupled dimers, more entangled PDC probes yield more spectroscopic information, even in the presence of emission into inaccessible modes. Moreover, simple, unentangled measurements can capture between 60% - 90% of the spectroscopic information. We thus establish that biphoton spectroscopy using source-engineered PDC probes and unentangled measurements can provide tangible quantum enhancement. Our work underscores the intricate role of entanglement in single-molecule spectroscopy using quantum light.

I. INTRODUCTION

Over the last couple of decades, entangled states of quantum light have been explored for their potential use in linear and nonlinear optical spectroscopy. Linear absorption spectroscopy in a ‘biphoton’ setup — employing a single one-photon interaction of the sample with the signal mode [1] of an entangled state — has been experimentally performed on glass [2], crystalline [3], and nanoparticle [4] samples. These offer a larger coincidence signal-to-noise ratio (SNR) compared to photon-counting measurements of classical light.

More recently, coherent non-linear optical spectroscopies using quantum light have been proposed and theoretically studied using a fully quantum mechanical approach [5]. Amongst these, two-photon absorption of entangled biphoton states has garnered much attention [5–11]. The supposed improved performance of these quantum spectroscopic methods over classical ones is often attributed to the availability of control variables such as the entanglement time that do not have classical counterparts [12], or more generally to the absence of the usual Fourier limit on joint temporal and spectral resolutions of entangled photons [5].

However, the improved SNR in the biphoton experiments may be attributed to the use of coincidence counters with sufficiently small time windows, and not to the inherent quantum correlations of the entangled, non-classical light. In fact, Stefanov has mathematically shown that probability distributions of outcomes of uncorrelated measurements on the two spatially distinguishable modes of the outgoing biphoton state can always be mimicked with

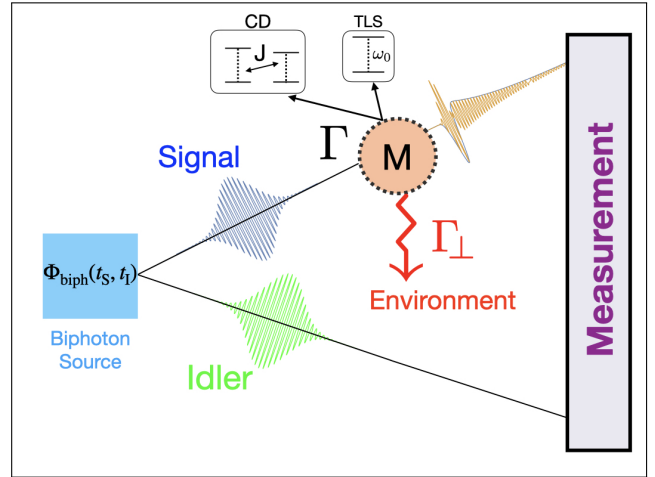


Figure 1. Schematic of pulsed biphoton spectroscopy. Only the signal photon interacts with the molecular system M , and both photons are measured after the light-matter interaction. Γ captures the interaction of M with the incoming signal mode while Γ_{\perp} does so for all other photonic modes, collectively dubbed the environment E . The specialisation of M to the two-level system (TLS) and coupled dimer (CD) is only made in Sections (VIB) and (VIC) respectively.

a ‘classical’ incoming ensemble with identical frequency correlations between the two photons, and *no* entanglement [1]. Entanglement with an additional ‘idler’ mode then seemingly provides no advantage, — or disadvantage, when the subsequent measurements on signal and idler modes are independent.

The general question of the role of entanglement in quantum light spectroscopy is more subtle and intricate. It depends on the location—at the input or at the measurement stage, on the model of the matter sample and the light-matter interaction, and on the nature and strength of

* aiman.khan.1@warwick.ac.uk

† animesh.datta@warwick.ac.uk

the coupling to both photonic and phononic environments. It also depends on the type of light used as probe (and consequently the type of entanglement, such as between time-frequency modes, photon numbers, or some other degrees of freedom), as well as on the time of measurement compared to the typical matter system timescale(s), its type, and the detection system used. Finally, it depends on what spectroscopy is defined to be. Mathematically, a larger probability — of absorption, emission, or general quantum measurement outcomes — is not identical to a higher precision of estimating unknown parameter(s) of the model matter system [13]. The latter is typically the operational goal of spectroscopy.

In this paper, we elucidate the role of time-frequency quantum entanglement in biphoton spectroscopy in the precise estimation of unknown parameters of individual molecules. As illustrated in Figure 1, it captures spectroscopic setups in which only one of the spatially distinct travelling modes interacts with the sample, the state of light itself carrying two excitations. Our interaction model is motivated by the coherent coupling of single molecules (with strength Γ) with optical fields. We also include a photonic environment characterised by the coupling strength Γ_{\perp} modelling emission into inaccessible modes. Our conclusions are based on the quantum information-theoretic methodology for quantum light spectroscopy developed in our recent paper [13].

Of proximate experimental relevance, we establish the functional utility of time-frequency entanglement for the spectroscopy of a two-level system (TLS) and a coupled dimer (CD) using states generated from weakly-pumped spontaneous parametric down conversion (PDC). Such states are typical of spectroscopic techniques employing entangled light [2–4, 6, 7, 9, 14, 15]. Our choice of matter systems also has immediate practical relevance. Under certain symmetries of the dipole operator or isotropic pumping, alkali-metal atomic vapours are approximately TLS [16]. The CD is often employed as a minimal model [17–19] for exciton-hopping quantum dynamics in a wide class of light-harvesting complexes such as the 8-site Fenna-Matthews-Olsen (FMO) complex and the 27-site B800-B850 light-harvesting-2 complexes. It is more substantively relevant for the cyanobacterial allophycocyanin (APC) complex [20], as well as conjugated polymers [21, 22].

Our main results for single-molecule biphoton spectroscopy are as follows:

1. At long times, the spectroscopic information is bounded by a sum of three — a two-photon, a one-photon, and a classical, contributions [Eq. (37)].
2. Entangled measurements across the signal and idler modes are not necessary to attain the bound in Eq. (37) [see Section (VA)].
3. Time-frequency entanglement of the input probe provides no in-principle advantage when $\Gamma_{\perp} = 0$ [see Section (VB)].
4. A class of optimised unentangled measurements always yield more information than any measurements on the signal photon state only [Eq. (52)], i.e., by tracing out the idler mode.
5. Time-frequency entanglement of PDC probes enhances the spectroscopy of TLS and CD systems. This can be used to engineer PDC sources for practical quantum-enhanced spectroscopy. [See Section (VI)].

Our results advance the understanding of single-molecule spectroscopy using entangled light. They pave the path towards capturing experimental scenarios that could be the successors of absorption-based techniques [23, 24] or fluorescence-based ones such as single-molecule pump-probe (SM2P) spectroscopy [25–27] using quantum light. To the best of our knowledge, all these single-molecule techniques have employed pulses of classical light, with or without a fixed phase relation between them. Our work also stand apart from other recent ones on “quantum-enhanced” spectroscopy that model the ensemble matter system as an infinite chain of beamsplitters [28–30].

In addition to treating both the light and matter quantum mechanically, our work advances the quantum-information theoretic understanding of spectroscopy using entangled light. It does so by clarifying the spectroscopic potential of entangled measurements across signal and idler modes, and a simpler class using local operations and classical communication (LOCC). These place our work beyond that of Stefanov [1].

The paper is structured as follows: in Section II, we recast quantum spectroscopy as a local estimation problem, which will be the basis of our evaluations of fundamental error bounds. In Section III, we describe the fully quantum model of pulsed light-matter interaction in biphoton spectroscopy, as well as define the form of the most general incoming biphoton probes that can be employed in the spectroscopic setup in Figure 1. In Section IV, we calculate explicit expressions for the quantum Fisher information (QFI) of the outgoing state for arbitrary incoming biphoton states and in the light-matter interaction Hamiltonian for the biphoton setup. In Section V, we will establish that unentangled measurements can attain the QFI, and also identify near-optimal measurements that should be more practical to implement. In Section VI, we apply the theoretical machinery of the previous sections to the experimentally viable PDC states, for which we also show that entanglement has a functional usefulness in TLS and CD spectroscopy. Finally, we conclude in Section VII.

II. QUANTUM LIGHT SPECTROSCOPY AS AN ESTIMATION PROBLEM

Spectroscopy uses light — quantum or classical, to probe matter systems via travelling field states. Following

the light-matter interaction, the probe(s) (P) carry away information about parameters of the matter (M) system. When both the light and the matter are described quantum mechanically, the quantum state of the probe light just before detection, can be generally represented as

$$\rho_{\text{out}}^{\text{P}}(\theta) = \text{Tr}_{\text{ME}}(\mathcal{V}_{\text{lm}}^{\theta}[\rho^{\text{M}} \otimes \rho^{\text{P}} \otimes |0^{\text{E}}\rangle\langle 0^{\text{E}}|]), \quad (1)$$

where ρ^{P} is the incoming probe state of light, ρ^{M} is the initial state of the matter system, $\mathcal{V}_{\text{lm}}^{\theta}$ captures the quantum interaction between light and matter and labelled by the single, real physical parameter θ that is to be estimated. $|0^{\text{E}}\rangle \equiv \bigotimes_l |0^l\rangle$ captures all environmental modes (E) of the electromagnetic field that may couple to the matter system M, unoccupied at the start of the experiment. The tracing out of the matter and the environmental modes captures the fact that these parts of the global state are inaccessible to the measurement apparatus.

The parametric model corresponding to POVM measurement $\{M_i : M_i > 0, \sum_i M_i = \mathbb{I}^{\text{P}}\}$ on the output state $\rho_{\text{out}}^{\text{P}}(\theta)$ is given by the Born rule $\{p(i|\theta) = \text{Tr}[\rho_{\text{out}}^{\text{P}}(\theta)M_i] | \theta \in \mathbb{R}\}$. Statistical inference then involves constructing estimators $\hat{\theta} = \theta(X_1, X_2, \dots, X_n)$, where $\{X_i\}$ are random variables corresponding to each of n measured values, independent and identically distributed. The variance of the estimator $V(\theta|\{M_i\}) = \mathbb{E}_{\theta}[(\hat{\theta} - \theta)^2]$ is the mean square error of the estimator statistic (\mathbb{E}_{θ} denotes expectation with respect to $X_1, X_2, \dots, X_n \sim p(i, \theta)$). It is upper-bounded by the Crámer-Rao bound (CRB) [31, 32]

$$V(\theta|\{M_i\}) \geq \frac{1}{n\mathcal{C}(\theta|\{M_i\})}, \quad (2)$$

and $\mathcal{C}(\theta|\{M_i\})$ is the (classical) Fisher information, defined as

$$\mathcal{C}(\theta|\{M_i\}) = \text{Var}_{\theta} \left[\frac{\partial}{\partial \theta} \log p(i|\theta) \right] = -\mathbb{E}_{\theta} \left[\frac{\partial}{\partial \theta} \log p(i|\theta) \right]^2. \quad (3)$$

The model, and therefore the optimal estimators themselves, depend on the POVM $\{M_i\}$.

A stronger and more fundamental bound on the precision of estimating θ can be obtained by minimising $V(\theta|\{M_i\})$ over all possible measurements $\{M_i\}$ allowed by the laws of quantum mechanics. This is referred to as the quantum Crámer-Rao bound (QCRB) [33, 34]

$$V(\theta|\{M_i\}) \geq \frac{1}{n\mathcal{C}(\theta|\{M_i\})} \geq \frac{1}{n\mathcal{Q}(\theta; \rho_{\text{out}}^{\text{P}}(\theta))}, \quad (4)$$

where $\mathcal{Q}(\theta; \rho_{\text{out}}^{\text{P}}(\theta))$ is the quantum Fisher information (QFI) corresponding to the parameter θ in the outgoing state $\rho_{\text{out}}^{\text{P}}(\theta)$,

$$\mathcal{Q}(\theta; \rho_{\text{out}}^{\text{P}}(\theta)) = \text{Tr}(\rho_{\text{out}}^{\text{P}}(\theta) L_{\theta}^2) \geq \mathcal{C}(\theta|\{M_i\}), \quad (5)$$

with the self-adjoint symmetric logarithmic derivative (SLD) operators defined via

$$L_{\theta} \rho_{\text{out}}^{\text{P}}(\theta) + \rho_{\text{out}}^{\text{P}}(\theta) L_{\theta} = 2 \frac{\partial \rho_{\text{out}}^{\text{P}}(\theta)}{\partial \theta}. \quad (6)$$

For the estimation of a single parameter θ , the corresponding QCRB can be saturated by the projective measurement corresponding to eigenvectors of the SLD operator L_{θ} [34]. For rank-deficient $\rho_{\text{out}}^{\text{P}}(\theta)$, however, this is only a necessary condition and eigenvectors of the SLD operator are only one of many QCRB-saturating POVMs [35]. Indeed, for pure states $\rho_{\text{out}}^{\text{P}}(\theta) = |\psi_{\theta}\rangle\langle \psi_{\theta}|$, the SLD operator has the simpler form

$$L_{\theta} = |\partial_{\theta}\psi_{\theta}\rangle\langle \psi_{\theta}| + |\psi_{\theta}\rangle\langle \partial_{\theta}\psi_{\theta}| \quad (7)$$

and the QFI is

$$\mathcal{Q}(\theta; \rho_{\text{out}}^{\text{P}}(\theta)) = 4 \left(\langle \partial_{\theta}\psi_{\theta} | \partial_{\theta}\psi_{\theta} \rangle - |\langle \psi_{\theta} | \partial_{\theta}\psi_{\theta} \rangle|^2 \right). \quad (8)$$

For a general mixed state expressed as its spectral decomposition, the QFI is [36, 37]

$$\begin{aligned} \mathcal{Q} \left(\theta; \sum_n p_n |\psi_n\rangle\langle \psi_n| \right) &= \sum_n \frac{(\partial_{\theta} p_n)^2}{p_n} \\ &+ \sum_n 4p_n \langle \partial_{\theta}\psi_n | \partial_{\theta}\psi_n \rangle - \sum_{m,n} \frac{8p_m p_n}{p_m + p_n} |\langle \partial_{\theta}\psi_m | \psi_n \rangle|^2. \end{aligned} \quad (9)$$

III. LIGHT-MATTER INTERACTION FOR A BIPHOTON PROBE

The dynamics of a quantum matter system interacting with quantised light can be described via the Hamiltonian

$$H = H^{\text{M}} + H^{\text{F}} + H^{\text{MSE}}, \quad (10)$$

where H^{M} corresponds to matter M dynamics only, H^{F} is the free field Hamiltonian corresponding to the incoming signal (S) and idler (I) modes, as well as the electromagnetic environmental E modes. Each term in H^{MSE} is of the dipole-field coupling form $-\mathbf{d} \cdot \mathbf{E}$, where \mathbf{d} is a transition dipole moment operator for the matter system, and \mathbf{E} is the (total) quantised electric field operator (see Figure 1). The dipole coupling term is appropriate for single molecules which are small compared to typical optical wavelengths, thus allowing the dipole approximation [38].

While our arguments can be extended to general molecular systems, we restrict our discussion in this paper to vibrationless P -site Hamiltonians ($P = 1, 2$) of the form

$$H^{\text{M}} = \sum_{j=1}^P \hbar\omega_j |j\rangle\langle j| + \sum_{i \neq j} J_{ij} |i\rangle\langle j|, \quad (11)$$

where $|j\rangle$ is the excited level corresponding to the j -th site (with frequency ω_j), and J_{ij} is the Coulomb dipole-dipole coupling between sites i and j . $P = 1$ corresponds to a two-level system (TLS) Hamiltonian, whereas $P = 2$ corresponds to the coupled dimer (CD) system, composed of two sites that are coupled to each other via the single coupling constant J . The transition dipole operator connecting the ground state of the matter system with the singly-excited manifold (SEM) is of the form

$\mathbf{d} = \sum_j (\boldsymbol{\mu}_{jg}|g\rangle\langle j| + \text{h.c.})$ where the matrix elements are $\boldsymbol{\mu}_{jg} = \langle g|\boldsymbol{\mu}|j\rangle$.

The free field Hamiltonian can be decomposed into a countably infinite number of one-dimensional (1-D) electromagnetic fields [39–42],

$$\begin{aligned} H^F &= \sum_{\epsilon} \int d^3\mathbf{k} \hbar c |\mathbf{k}| a_{\epsilon}^{\dagger}(\mathbf{k}) a_{\epsilon}(\mathbf{k}) \\ &= \sum_l \int_0^{\infty} d\omega \hbar \omega a_l^{\dagger}(\omega) a_l(\omega), \end{aligned} \quad (12)$$

where \mathbf{k} and ϵ are respectively the wavevector and polarisation indices for the electromagnetic mode, and the subsequent index l labels the resulting 1-D modes. Although the sum over the index l necessarily runs to infinity and subsumes both the incoming signal/idler modes, as well as the environmental E modes, we only need consider, in the description of the light-matter interaction, modes that couple to the matter system M due to H^{MSE} itself.

These modes can be identified using the slowly-varying envelope approximation (SVEA) in the optical domain, where the frequency bandwidth of the incoming field is assumed to be much smaller than the carrier wave frequency $B \ll \bar{\omega}_S$. Furthermore, the propagating, incoming beam of the signal S arm can be approximated to be paraxial. 1-D quantisation of the solutions of the classical paraxial equation for the signal arm along the direction of propagation yields [43]

$$\mathbf{E}_S(t) = i\epsilon_S \mathcal{A}_S(\bar{\omega}_S) \int_{-\infty}^{\infty} d\omega_S a_S(\omega_S) e^{-i\omega_S t}, \quad (13)$$

where $\mathcal{A}_S(\bar{\omega}_S) = \sqrt{\frac{\bar{\omega}_S}{2\epsilon_0 c A \hbar}}$ is the collective pulse factor (A is the transverse quantisation area of the signal beam), and ϵ_S denotes the unit polarisation vector of the signal beam. Note that the emergent Fourier transform of the field operators can be notated as

$$a_S(t) = \frac{1}{\sqrt{2\pi}} \int_{-\infty}^{\infty} d\omega_S a_S(\omega_S) e^{-i\omega_S t}. \quad (14)$$

These are known as white-noise operators and are δ -correlated in time as $[a_S(t), a_S^{\dagger}(t')] = \delta(t - t')$, where $\delta(t)$ is the Dirac delta function.

Description of the electromagnetic environment E is simplified by the practical fact that they are inaccessible to experiments, and must be considered in terms of their effects on reduced dynamics only. This effect can then be recovered by using a single bosonic degree of freedom (as opposed to the infinitude of environmental spatial modes that the matter system M may decay into), labelled by the ‘ b ’ operators:

$$\mathbf{E}_E(t) = i\epsilon_E \mathcal{A}_E(\bar{\omega}_S) \int_{-\infty}^{\infty} d\omega_E b(\omega_E) e^{-i\omega_E t}, \quad (15)$$

where $\mathcal{A}_E(\bar{\omega}_S)$ is a collective factor characterising the effect of the continuum electromagnetic environment. For a more detailed description, see Ref. [13, Appendix A].

In the interaction frame generated by $H_0 = \sum_j \hbar \bar{\omega}_S |j\rangle\langle j| + H^F$, where the field Hamiltonian can be taken to include only modes that participate in the interaction

$$H^F = \int d\omega \hbar \omega a_S^{\dagger}(\omega) a_S(\omega) + \int d\omega \hbar \omega b^{\dagger}(\omega) b(\omega), \quad (16)$$

the total Hamiltonian of the biphoton setup in Figure 1 is

$$\begin{aligned} H(t) &= H_I^M - i\hbar (\sqrt{\Gamma} L^{\dagger} \otimes a_S(t) \otimes \mathbb{1}^I \otimes \mathbb{1}^E \\ &\quad + \sqrt{\Gamma_{\perp}} L^{\dagger} \otimes \mathbb{1}^S \otimes \mathbb{1}^I \otimes b(t) - \text{h.c.}), \end{aligned} \quad (17)$$

where $H_I^M = \sum_j \hbar(\omega_j - \bar{\omega}_S) + \sum_{j \neq k} J_{jk} |j\rangle\langle k|$, and $\mathbb{1}^S$ ($\mathbb{1}^I$) is identity operator on the signal (idler) Hilbert space. Further, the collective dipole operators, weighted by the strength of interaction, are

$$\begin{aligned} \sqrt{\Gamma} L &= \sqrt{2\pi} \mathcal{A}_S(\bar{\omega}_S) \sum_j \frac{(\epsilon_S \cdot \boldsymbol{\mu}_{jg})}{\hbar} |g\rangle\langle j|, \\ \sqrt{\Gamma_{\perp}} L &= \sqrt{2\pi} \mathcal{A}_E(\bar{\omega}_S) \sum_j \frac{(\epsilon_E \cdot \boldsymbol{\mu}_{jg})}{\hbar} |g\rangle\langle j|. \end{aligned} \quad (18)$$

1. Incoming Probe State of Entangled Light

An arbitrary incoming biphoton state in terms of continuous frequency variables ω_S and ω_I , corresponding to signal and idler modes respectively, can be expressed as

$$|\Phi_{\text{biph}}\rangle = \int d\omega_S \int d\omega_I \tilde{\Phi}(\omega_S, \omega_I) a_S^{\dagger}(\omega_S) a_I^{\dagger}(\omega_I) |0\rangle \quad (19)$$

where $\tilde{\Phi}(\omega_S, \omega_I)$ is the joint spectral amplitude (JSA) of the entangled state in frequency space, and contains all two-photon correlations. The bivariate JSA function admits a Schmidt decomposition [44]

$$\tilde{\Phi}(\omega_S, \omega_I) = \sum_n r_n \tilde{\xi}_n^S(\omega_S) \tilde{\xi}_n^I(\omega_I), \quad (20)$$

which in turn can be used to express the biphoton state in Eq. (19) in terms of discrete orthonormal Schmidt modes

$$|\Phi_{\text{biph}}\rangle = \sum_n r_n a_{n,S}^{\dagger} a_{n,I}^{\dagger} |0\rangle \equiv \sum_n r_n |\xi_n^S\rangle |\xi_n^I\rangle, \quad (21)$$

where

$$a_{n,S}^{\dagger} = \int d\omega_S \tilde{\xi}_n^S(\omega_S) a_S^{\dagger}(\omega_S), \quad a_{n,I}^{\dagger} = \int d\omega_I \tilde{\xi}_n^I(\omega_I) a_I^{\dagger}(\omega_I), \quad (22)$$

are Schmidt mode creation operators, and $|\xi_n^X\rangle = a_{n,X}^{\dagger} |0\rangle$, $X = S, I$ are the corresponding Schmidt basis kets.

We make the additional assumption that the idler spectral amplitude is peaked around a central frequency

$\bar{\omega}_I$, so that $a_I^\dagger(\omega_I) \rightarrow a_I^\dagger(\omega_I - \bar{\omega}_I)$ yields idler operators peaked around $\omega_I = 0$. This is justified if the biphoton entangled states are produced in physical processes in which (one or more) pump pulse photons, derived from a spectral amplitude distribution centred around some central frequency $\bar{\omega}_P$, are converted into daughter signal (centred around $\bar{\omega}_S$) and idler (centred around $\bar{\omega}_I$) photons. For biphoton states produced in the weak downconversion limit of type-II spontaneous PDC using $\chi^{(2)}$ -nonlinear crystals, conservation of energy dictates that $\bar{\omega}_P = \bar{\omega}_S + \bar{\omega}_I$. On the other hand, for biphoton states produced in four-wave mixing (FWM) schemes [45–47] that exploit $\chi^{(3)}$ -nonlinearities, conservation of energy dictates (for degenerate schemes) that $2\bar{\omega}_P = \bar{\omega}_S + \bar{\omega}_I$. This assumption is distinct from the SVEA, and is motivated by the details of the physical process used to produce the biphoton entangled state. In terms of the re-centred signal and idler field operators, the JSA of the biphoton state in Eq. (19) then correspondingly transforms as $\tilde{\Phi}_{\text{biph}}(\omega_S, \omega_I) \rightarrow \tilde{\Phi}_{\text{biph}}(\omega_S - \bar{\omega}_S, \omega_I - \bar{\omega}_I)$.

In the rest of this paper, we assume that the JSA function $\tilde{\Phi}_{\text{biph}}(\omega_S, \omega_I)$, as well as photon operators $a_S^\dagger(\omega_S)$ and $a_I^\dagger(\omega_I)$ to have been appropriately re-centred so that $\bar{\omega}_S = \bar{\omega}_I = 0$. Positing corresponding white noise operators obtained as Fourier transforms of centred idler operators, $a_I^\dagger(t_I) = \frac{1}{\sqrt{2\pi}} \int d\omega_I e^{-i\omega_I t_I} a_I^\dagger(\omega_I)$, we can obtain an equivalent representation of the biphoton entangled state in terms of operators $a_S^\dagger(t)$ and $a_I^\dagger(t)$,

$$|\Phi_{\text{biph}}\rangle = \int dt_S \int dt_I \Phi_{\text{biph}}(t_S, t_I) a_S^\dagger(t_S) a_I^\dagger(t_I) |0\rangle, \quad (23)$$

where the time-axis joint temporal amplitude (JTA) $\Phi_{\text{biph}}(t_S, t_I)$ is the two-dimensional Fourier transform of the centred frequency-axis JSA $\tilde{\Phi}(\omega_S, \omega_I)$,

$$\Phi_{\text{biph}}(t_S, t_I) = \frac{1}{2\pi} \int d\omega_S \int d\omega_I e^{i(\omega_S t_S + \omega_I t_I)} \tilde{\Phi}_{\text{biph}}(\omega_S, \omega_I). \quad (24)$$

The JTA $\Phi_{\text{biph}}(t_S, t_I)$ then admits an analogous Schmidt decomposition

$$\Phi_{\text{biph}}(t_S, t_I) = \sum_n r_n \xi_n^S(t_S) \xi_n^I(t_I), \quad (25)$$

where

$$\xi_n^X(t_X) = \frac{1}{\sqrt{2\pi}} \int d\omega_X e^{i\omega_X t_X} \tilde{\xi}_n^X(\omega_X), \quad X = S, I, \quad (26)$$

are the time-domain Schmidt basis functions.

IV. QFI FOR A BIPHOTON PROBE

We start with the molecule in its ground state $|g\rangle\langle g|$ at $t = 0$. Then, the joint SI-E state at asymptotically long times t , where $\max[\Gamma, \Gamma_\perp]t \gg 1$, is effected by the

completely-positive, trace-preserving (CPTP) map

$$\mathcal{W}_g[\rho^{\text{SI}} \otimes |0^E\rangle\langle 0^E|] = \text{Tr}_M \left[\lim_{t \rightarrow \infty} U(t) |g\rangle\langle g| \otimes \rho^{\text{SI}} \otimes |0^E\rangle\langle 0^E| U^\dagger(t) \right], \quad (27)$$

where $U(t) = \mathcal{T} \left[\exp \left(-\frac{i}{\hbar} \int_{-\infty}^t dt' H(t') \right) \right]$ is the unitary propagator corresponding to Eq. (17), and ρ^{SI} is the signal-idler probe state. At $t \rightarrow \infty$, the molecule decays back to the ground state $|g\rangle$. Thus, for a pure biphoton input $\rho^{\text{SI}} = |\Phi_{\text{biph}}\rangle\langle \Phi_{\text{biph}}|$, the transformed state $\mathcal{W}_g [|\Phi_{\text{biph}}\rangle\langle \Phi_{\text{biph}}| \otimes |0^E\rangle\langle 0^E|]$ is also pure. The linearity of the CPTP map \mathcal{W}_g can be employed to obtain the outgoing SI-E state as the piecewise transformation of the Schmidt component wavefunctions on the signal-environment SE subspace, while the idler I components remain unchanged, giving

$$\begin{aligned} \mathcal{W}_g \left[\sum_n r_n |\xi_n^S\rangle |\xi_n^I\rangle \otimes |0^E\rangle \right] &= \sum_n r_n \mathcal{W}_g [|\xi_n^S\rangle |\xi_n^I\rangle \otimes |0^E\rangle] \\ &= \sum_n r_n (|\phi_n^S\rangle |\xi_n^I\rangle \otimes |0^E\rangle + |0^S\rangle |\xi_n^I\rangle \otimes |\pi_n^E\rangle), \end{aligned} \quad (28)$$

where the first term captures the signal photon being emitted into its original mode after absorption, while the second captures the absorbed signal photon being emitted into the environment. Here, the n -th components

$$|\phi_n^S\rangle = |\xi_n^S\rangle - \Gamma |\varepsilon_n^S\rangle, \quad |\pi_n^E\rangle = -\sqrt{\Gamma\Gamma_\perp} |\varepsilon_n^E\rangle \quad (29)$$

are obtained using the single-mode solutions [48] as used in Ref. [13]. We have abbreviated the distortion in the n -th Schmidt mode of the signal space as

$$|\varepsilon_n^S\rangle = \int_{-\infty}^{\infty} dt_1 \left[\int_{-\infty}^{t_1} d\tau f_M(t_1 - \tau) \xi_n^S(\tau) \right] a_S^\dagger(t_1) |0\rangle, \quad (30)$$

where

$$f_M(t) = \langle g| L \exp \left[\left(-iH_I^M - \frac{\Gamma + \Gamma_\perp}{2} L^\dagger L \right) t \right] L^\dagger |g\rangle \quad (31)$$

is the characteristic response function of the molecule M. Analogous definitions can be made for $|\varepsilon_n^E\rangle$.

Partial trace over the E subspace yields the outgoing state as the mixture of single photon (in the idler mode) and biphoton states,

$$\rho_{\text{biph,out}}^{\text{SI}} = (1 - N) |\Phi_{\text{biph,out}}\rangle\langle \Phi_{\text{biph,out}}| + N |0^S\rangle\langle 0^S| \otimes \sigma^I \quad (32)$$

where

$$|\Phi_{\text{biph,out}}\rangle = \frac{1}{\sqrt{1 - N}} \sum_n r_n |\phi_n^S\rangle |\xi_n^I\rangle, \quad (33)$$

the normalisation factor being $N = \Gamma\Gamma_\perp \sum_n r_n^2 \langle \varepsilon_n^S | \varepsilon_n^S \rangle$, and

$$\sigma^I = \frac{\Gamma\Gamma_\perp}{N} \sum_{mn} r_m r_n \langle \varepsilon_m^E | \varepsilon_m^E \rangle |\xi_m^I\rangle \langle \xi_n^I| \quad (34)$$

is the conditional idler state when the excitation due to the signal is lost to E. Note that the transformed signal states are no longer orthonormal

$$\langle \phi_m^S | \phi_n^S \rangle = \delta_{mn} - \Gamma \Gamma_{\perp} \langle \varepsilon_m^S | \varepsilon_n^S \rangle. \quad (35)$$

This is, however, recovered in the limit of perfect coupling so that $\lim_{\Gamma_{\perp} \rightarrow 0} \langle \phi_m^S | \phi_n^S \rangle = \delta_{mn}$. As $\sigma^{\text{SI}} = |0^{\text{S}}\rangle\langle 0^{\text{S}}| \otimes \sigma^{\text{I}}$ has no excitation in the S space, whereas $|\Phi_{\text{biph,out}}\rangle$ does, the two contributions Eq. (33) to the mixture live in mutually orthogonal subspaces. Thus,

$$\langle \Phi_{\text{biph,out}} | \sigma^{\text{SI}} | \Phi_{\text{biph,out}} \rangle = 0 \quad (36)$$

yielding the form of the QFI [36] of the outgoing state with respect to the Hamiltonian parameter θ as

$$\mathcal{Q}(\theta; \rho_{\text{biph,out}}^{\text{SI}}) = \mathcal{C}(N, 1 - N) + N\mathcal{Q}(\theta; \sigma^{\text{I}}) + (1 - N)\mathcal{Q}(\theta; |\Phi_{\text{biph,out}}\rangle), \quad (37)$$

where $\mathcal{C}(N, 1 - N) = N_{\theta}/N(1 - N)$ (with $N_{\theta} \equiv \partial_{\theta}N$) is the Fisher information associated with classical mixing of the $|\Phi_{\text{biph,out}}\rangle$ and $|0^{\text{S}}\rangle\langle 0^{\text{S}}| \otimes \sigma^{\text{I}}$ quantum states. The conditional idler QFI $\mathcal{Q}(\theta; \sigma^{\text{I}})$ can be obtained by solving Eq. (6) for σ^{I} , and using Eq. (5). The biphoton QFI term can be shown to be (for details, see Appendix A)

$$\begin{aligned} \mathcal{Q}(\theta; |\Phi_{\text{biph,out}}\rangle) &= \frac{1}{1 - N} \sum_n |r_n|^2 \langle \partial_{\theta} \phi_n^S | \partial_{\theta} \phi_n^S \rangle \\ &\quad - \frac{1}{(1 - N)^2} \left| \sum_n |r_n|^2 \langle \phi_n^S | \partial_{\theta} \phi_n^S \rangle \right|^2. \end{aligned} \quad (38)$$

Eq. (37) is one of our main results, that the spectroscopic information about the molecule M has three distinct contributions - from the biphoton state whose signal mode is modified by its interaction with M, the one-photon idler state when the absorbed photon is lost to E, and finally the classical mixture of the two.

In the absence of entanglement, that is a product JSA where $r_n = 0 \forall n > 1$, $\sigma^{\text{I}} = \mathbb{1}^{\text{I}}$, and $\mathcal{Q}(\theta; \sigma^{\text{I}}) = 0$. Eq. (37) then reduces to single-photon spectroscopy [13].

In the presence of entanglement, the contributions of the three terms in Eq. (37) depend on the relative magnitudes of M-S and M-E coupling. These corresponds to different flavours of experimental setups — in free space scenarios where $\Gamma_{\perp} \gg \Gamma$, the first two terms dominate in Eq. (37) as most of the signal excitation are lost to the E space. In contrast, for geometries engineered such that $\Gamma_{\perp} \ll \Gamma$, the biphoton QFI will be the major contributor as few excitations are lost to E. This is summarised in Table I.

A. Attaining the QFI in Eq. (37)

The three terms in Eq. (37) may be successively saturated in a cascade of mutually commuting measurements on orthogonal subspaces in the SI space as illustrated schematically in Figure 2 (a).

Γ_{\perp}/Γ	$\mathcal{C}(N, 1 - N)$	$N\mathcal{Q}(\sigma^{\text{I}})$	$(1 - N)\mathcal{Q}(\Phi_{\text{biph,out}}\rangle)$
$\ll 1$	×	×	✓
$O(1)$	✓	✓	✓
$\gg 1$	✓	✓	×

Table I. Dominant contributions to spectroscopic information QFI $\mathcal{Q}(\theta; \rho_{\text{biph,out}}^{\text{SI}})$ in the asymptotic time limit $t \rightarrow \infty$ for different regimes of relative M-S and M-E couplings. A fuller dependance on the relative magnitudes of M-S coupling Γ and M-E coupling Γ_{\perp} is provided in Appendix B.

The first term $\mathcal{C}(N, 1 - N)$ can be attained using quantum non-demolition (QND) photon counting measurement effected by the set of signal projectors $\{\Pi_0^{\text{S}}, \Pi_1^{\text{S}}\}$, where $\Pi_0^{\text{S}} = |0^{\text{S}}\rangle\langle 0^{\text{S}}|$, and $\Pi_1^{\text{S}} = \int d\omega a_{\text{S}}^{\dagger}(\omega)|0^{\text{S}}\rangle\langle 0^{\text{S}}|a_{\text{S}}(\omega)$. A QND measurement is advisable as destructive photon counting at this stage can only fetch as much as the information as the classical $\mathcal{C}(N, 1 - N)$ term, the collapsed photon states carrying no more quantum information. Practically, such QND photon counting has been achieved using either cross-Kerr mapping of photons numbers onto phase shifts of a secondary optical probe [49–51], or by strongly coupling the photonic state to atoms in cavity electrodynamics that maps photon numbers to atomic phases, which can then be detected using interferometric techniques [52–54]. The photon counting measurements, non-demolition or not, are effectively absorption measurements, and the magnitude of N can be estimated from these measurement outcomes

The second term $N\mathcal{Q}(\sigma^{\text{I}})$ can, in general, be attained by measuring (idler) projectors corresponding to the eigenvectors of the SLD for σ^{I} . A practical setup that can implement approximately optimal single-photon projectors as mode-resolved photon counting may be achieved using quantum pulse gating (QPG) techniques [55–60] for ultrafast pulses. This involves an incoherent train of pulses coupling with a sufficiently shaped gating pulse in a sum-frequency interaction inside a nonlinear crystal. The shape of the gating pulse determines the mode the incoming pulse is effectively projected on to, presenting at the output as a higher frequency signal than the incoming pulse (see Figure 2 (b)).

The third term in Eq. (37) may, in general require measurements entangled across the signal and idler on the pure state $|\Phi_{\text{biph,out}}\rangle$ to be attained. In the next section, we show that an unentangled measurement suffices.

V. 1-LOCC DETECTION SCHEMES

Measurement protocols for multipartite quantum systems can be divided into three classes [61, 62] — (a) uncorrelated local measurements (LM) with no classical communication between individual substations, (b) correlated local operations and classical communication (LOCC) where results of local measurement operations may be conveyed back and forth between the various substations using classical bits, and (c) global measurements (GM)

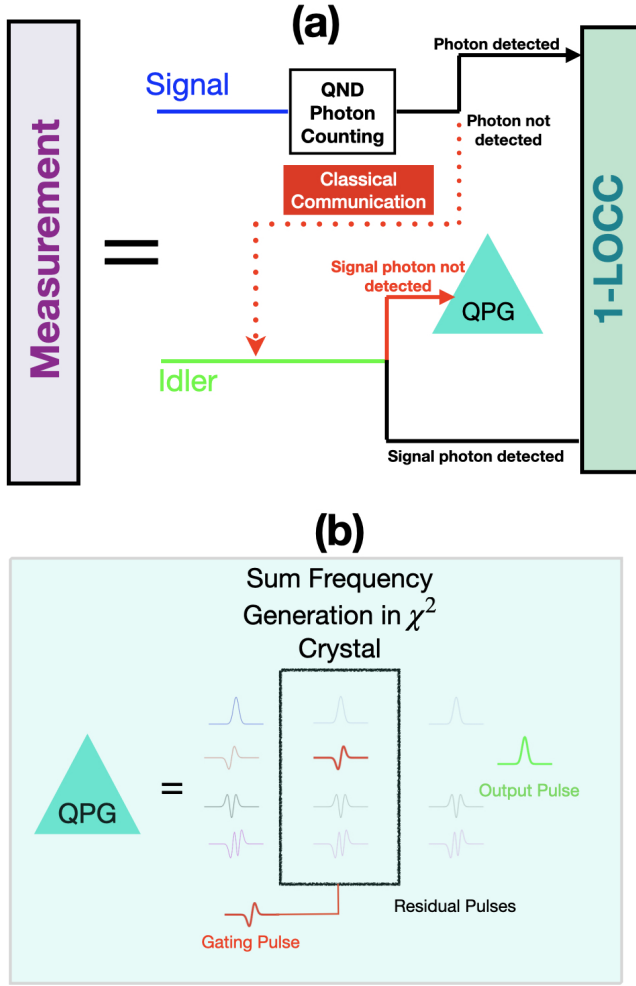


Figure 2. Detection scheme that fetches estimator precision corresponding to full QFI in Eq. (37). (a) Schematic of cascade of mutually admissible measurements. As a first step, QND photon counting is performed on the signal substation. Based on the outcome (classically communicated to the idler substation), the idler photon is either detected in mode-resolved projective measurement, or sent to the 1-LOCC box, which is discussed in detail in Section V (schematic illustration in Figure 3). (b) QPG implementation of mode-resolved photon counting.

which are the most general class of measurements that can be performed on multipartite quantum systems. In terms of their ability to extract quantum information and resource intensiveness of practical implementation [63], $\text{LM} \subseteq \text{LOCC} \subseteq \text{GM}$. In our spectroscopic setup, entangled measurements across the signal and the idler would be in GM, but not LM or LOCC.

We show that such entangled measurements are *not* necessary to attain the third term in Eq. (37). In fact, we show that a one-way idler-to-signal LOCC measurement scheme — that we will henceforth refer to as “1-LOCC”, always attains the third term in Eq. (37). For the biphoton setup, the most general 1-LOCC is schematically illus-

trated in Figure 3. In such a detection scheme, the results of local measurement on the idler substation, are classically communicated on to the signal substation, where then measurement operators for local detection are chosen accordingly¹. This is another of our main results.

Experimentally, LOCC operations on continuous-variable (CV) time-frequency entangled states have been successfully implemented as part of CV teleportation of light states [64, 65]. Our 1-LOCC detection scheme is thus a potentially attractive class of measurements for biphoton spectroscopy, and must be contrasted against interferometric quantum spectroscopies that propose global measurements by bringing together the two photons in linear [66, 67] or non-linear interferometers [68] at the detection stage.

Operationally, the idler-to-signal 1-LOCC detection scheme can also be viewed as a heralding scheme where a measurement is performed on the idler photon, and outcomes communicated to the signal station independently of the light-matter interaction which has support on the MSE subspace.

We construct a spectroscopically useful subclass of 1-LOCC detection schemes by optimising the CFI over POVMs on the signal mode only. We call this the “measurement-optimal” 1-LOCC detection scheme, and show that it (i) always includes a measurement whose CFI equals $\mathcal{Q}(\theta; |\Phi_{\text{biph,out}}(\theta)\rangle)$ in a specific choice of the 1-LOCC scheme, and (ii) the associated CFI for *all* members exceeds that of any single-photon measurement on the reduced signal state only.

For perfect coupling geometries ($\Gamma_{\perp} = 0$), (i) implies that entanglement in the incoming biphoton state is not, in-principle, a resource. This is because the QFI of an entangled biphoton state may be attained with a suitably heralded Fock state and uncorrelated LM measurement.

A. 1-LOCC Fisher Information in Biphoton Setup

The most general idler-to-signal 1-LOCC detection scheme proceeds in the following three steps:

1. Projectively measure the idler photon in the basis $\{V|\xi_x^I\rangle\langle\xi_x^I|V^\dagger\}$, where V is an arbitrary unitary operator on the idler Hilbert space. This transforms the incoming entangled biphoton probe state via

¹ Signal-to-idler 1-LOCC detection schemes can be constructed in similar fashion, but with some important differences. See Appendix C. Signal-to-idler schemes may be more challenging to implement practically as the preparation step must necessarily follow the light-matter interaction, outcomes of which must subsequently be communicated to the idler substation.

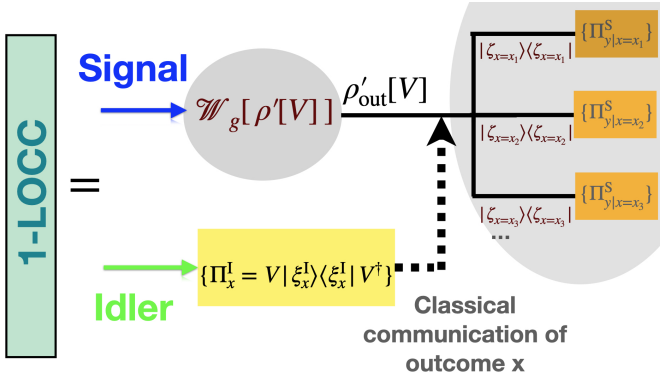


Figure 3. Idler-to-signal 1-LOCC scheme. The biphoton Kraus operators for the overall LOCC scheme are given as $\{\Pi_{y,x} = \Pi_{y|x}^S \otimes \Pi_x^I\}$.

Kraus operators $\Pi_x^I = \mathbb{1}^S \otimes V |\xi_x^I\rangle \langle \xi_x^I| V^\dagger$ to

$$\begin{aligned} \rho'[V] &= \sum_x (\Pi_x^I)^\dagger |\Phi_{\text{biph}}\rangle \langle \Phi_{\text{biph}}| \Pi_x^I \\ &= \sum_x |\psi_x\rangle \langle \psi_x| \otimes V |\xi_x^I\rangle \langle \xi_x^I| V^\dagger, \end{aligned} \quad (39)$$

where $|\psi_x\rangle = \sum_n r_n V_{nx}^* |\xi_n^S\rangle$, and $V_{mn} = \langle \xi_m^I | V | \xi_n^I \rangle$ are elements of unitary matrix V in the idler Schmidt basis.

2. Communicate (classically) the outcome of projective measurement $\{\Pi_x^I\}$ to the signal substation. The M-S-E interaction, given by the CPTP map \mathcal{W}_g in Eq. (27), transforms the signal Schmidt basis $\{|\xi_n^S\rangle\}$ onto the non-orthonormal set² $\{|\phi_n^S\rangle\}$, and renormalises the outgoing state as in Eq. (33). The resulting SI state is given by

$$\rho'_{\text{out}}[V] = \sum_x |\zeta_x\rangle \langle \zeta_x| \otimes V |\xi_x^I\rangle \langle \xi_x^I| V^\dagger, \quad (40)$$

where $|\zeta_x\rangle = \frac{1}{\sqrt{1-N}} \sum_n r_n V_{nx}^* |\phi_n^S\rangle$, is the unnormalised conditional signal state for the outcome x .

3. Measure the signal photon using operators $\{\Pi_{y|x=x_m}^S\}$ depending on the communication $x = x_m$ received from the idler.

These stages of the 1-LOCC scheme are illustrated in Figure 3.

² The preparation step (characterised by Kraus operators $\{\Pi_x^I\}$) quantum operation and the M-S-E interaction (characterised by superoperator \mathcal{W}_g) commute with each other, and can be applied in any order. If, in the final step, the signal subensembles $\{|\zeta_x\rangle\}$ are all projected onto a common measurement basis, the LOCC scheme reduces to an LM scheme with independent measurements performed at signal and idler substations.

The maximum CFI attainable using a 1-LOCC scheme is formally given by

$$\begin{aligned} &\max_{\Pi_{y|x}^S, \Pi_x^I} \mathcal{C}(\theta | \{\Pi_{y,x} = \Pi_{y|x}^S \otimes \Pi_x^I\}) \\ &= \max_{\Pi_x^I} \left(\max_{\Pi_{y|x}^S} \mathcal{C}(\theta | \{\Pi_{y,x} = \Pi_{y|x}^S \otimes \Pi_x^I\}) \right), \end{aligned} \quad (41)$$

s.t. $\sum_x \Pi_x^I = \mathbb{1}^I$, $\sum_y \Pi_{y|x}^S = \mathbb{1}^S \forall x$. The maximal 1-LOCC CFI is upper bounded as

$$\max_{\Pi_{y|x}^S, \Pi_x^I} \mathcal{C}(\theta | \{\Pi_{y,x} = \Pi_{y|x}^S \otimes \Pi_x^I\}) \leq \mathcal{Q}(\theta; |\Phi_{\text{biph,out}}\rangle). \quad (42)$$

since $1\text{-LOCC} \subseteq \text{LOCC} \subseteq \text{GM}$.

The maximisation of the CFI functional may now proceed in two steps, following the RHS of Eq. (41): first, for a given unitary V , the CFI is maximised over all allowed $\{\Pi_{y|x=x_m}^S\}$, and second, the resulting quantity is maximised over all $\Pi_x^I = \mathbb{1}^S \otimes V |\xi_x^I\rangle \langle \xi_x^I| V^\dagger$, which amounts to a maximisation over all unitary operations V . All 1-LOCC for which maximisation over signal POVM $\{\Pi_{y|x=x_m}^S\}$ has been performed will be termed ‘‘measurement-optimal’’, and the corresponding CFI quantity, now just a function of the preparation unitary V , is given as

$$\mathcal{C}_{\text{max}}(\theta; V) = \max_{\Pi_{y|x}^S} \mathcal{C}(\theta | \{\Pi_{y,x} = \Pi_{y|x}^S \otimes \Pi_x^I\}). \quad (43)$$

Constructing the orthogonal complement of $|\Phi_{\text{biph,out}}\rangle$ in the two-dimensional $\text{Span}[|\Phi_{\text{biph,out}}\rangle, |\partial_\theta \Phi_{\text{biph,out}}\rangle]$ as [35]

$$|\Phi_{\text{biph,out}}^\perp\rangle \equiv (1 - |\Phi_{\text{biph,out}}\rangle \langle \Phi_{\text{biph,out}}|) |\partial_\theta \Phi_{\text{biph,out}}\rangle, \quad (44)$$

the following result holds:

Theorem 1. For a preparation step unitary V_0 that satisfies

$$\langle \xi_m^I | V_0^\dagger \text{Tr}_S |\Phi_{\text{biph,out}}\rangle \langle \Phi_{\text{biph,out}}^\perp | V_0 | \xi_m^I \rangle = 0 \quad \forall m, \quad (45)$$

$$\mathcal{C}_{\text{max}}(\theta; V_0) = \mathcal{Q}(\theta; |\Phi_{\text{biph,out}}\rangle).$$

A proof appears in Appendix D.

A constructive proof for the existence of a V_0 satisfying Eq. (45) has been established for finite dimensions [62, 69]. It can be extended to trace-class (and hence bounded and compact) operators on CV spaces, including $\text{Tr}_S |\Phi_{\text{biph,out}}\rangle \langle \Phi_{\text{biph,out}}^\perp |$ in Eq. (45).

Following the upper bound in Eq. (42), the measurement-optimal 1-LOCC characterised by V_0 must correspond to the maximal CFI attainable. Thus, the biphoton component of the QFI in Eq. (37) may be attained in a measurement-optimal 1-LOCC scheme with $V_{\text{opt}} = V_0$ — that is, an unentangled measurement. The unitary V_0 , in general, depends on the the outgoing signal modes $\{\phi_n^S\}$, which themselves change with the nature and strength of M-S and M-E interactions.

B. No advantage from entangled input probe

If $\Gamma_{\perp} = 0$, only the third term in Eq. (37) survives. Then there always exists a single-photon Fock state

$$|\zeta_{x_m}^{\text{opt},'}\rangle = \frac{1}{\sqrt{\langle \zeta_{x_m}^{\text{opt}} | \zeta_{x_m}^{\text{opt}} \rangle}} |\zeta_{x_m}^{\text{opt}}\rangle, \quad (46)$$

where

$$|\zeta_{x_m}^{\text{opt}}\rangle = \frac{1}{\sqrt{1-N}} \sum_n r_n (V_{\text{opt}})_{nx_m}^* |\phi_n^S\rangle \quad (47)$$

for some measurement outcome $x = x_m$, which has at least as much QFI as the entangled input in Eq. (19). In principle, time-frequency entanglement of the input thus provides no advantage in this scenario.

This follows from Theorem 1, whereby the biphoton QFI can be written as the convex combination of signal-only QFIs as (see Eqs. (D3) and (D21) in Appendix D)

$$\mathcal{Q}(\theta; |\Phi_{\text{biph,out}}\rangle) = \sum_x \langle \zeta_x^{\text{opt}} | \zeta_x^{\text{opt}} \rangle \mathcal{Q}(\theta; |\zeta_x^{\text{opt},'}\rangle) \quad (48)$$

where $|\zeta_x^{\text{opt},'}\rangle = \frac{1}{\sqrt{\langle \zeta_x^{\text{opt}} | \zeta_x^{\text{opt}} \rangle}} |\zeta_x^{\text{opt}}\rangle$ are normalised conditional states. Equivalently, the biphoton QFI is always equal to the QFI of the following separable state

$$\begin{aligned} & \mathcal{Q}(\theta; |\Phi_{\text{biph,out}}\rangle) \\ &= \mathcal{Q}\left(\theta; \sum_x |\zeta_x^{\text{opt}}\rangle \langle \zeta_x^{\text{opt}}| \otimes V_{\text{opt}} |\xi_x^I\rangle \langle \xi_x^I| V_{\text{opt}}^\dagger\right). \end{aligned} \quad (49)$$

This shows that it is always possible to engineer the incoming state of light so as to prepare deterministically the product state component in the convex sum in Eq. (48) with the maximal QFI $\max_x \mathcal{Q}(\theta; |\zeta_x^{\text{opt},'}\rangle)$ (which we will label by index $x = x_m$) so that the QFI of the separable state then yields at least as much precision as the entangled biphoton state.

Operationally, one need only start then with the (pre-conditioned) single-photon signal state

$$|\psi_{x_m}^{\text{opt}}\rangle = \frac{1}{\sqrt{1-N}} \sum_n (V_{\text{opt}})_{nx_m}^* |\xi_n^S\rangle, \quad (50)$$

which would yield the outgoing state $|\zeta_{x_m}^{\text{opt},'}\rangle$ whose QFI is always greater than, or equal to, the biphoton QFI $\mathcal{Q}(\theta; |\Phi_{\text{biph,out}}\rangle)$.

This subsection extends a similar conclusion in Ref. [13] for the restricted case of resonant Γ -estimation in TLS for $\Gamma_{\perp} = 0$ to an arbitrary Hamiltonian parameter θ .

Our conclusion that an entangled input is not, in-principle, a resource can also be extended to scenarios with $\Gamma_{\perp} \neq 0$ when the biphoton state $|\Phi_{\text{biph,out}}\rangle$ is post-selected, because, in that case the first two terms in Eq. (37) drop out. The question of whether an entangled input is advantageous when all the three terms in Eq. (37) contribute, however, remains open.

C. Lower Bound on Measurement-Optimal Protocols

For any measurement-optimal 1-LOCC CFI,

$$\begin{aligned} \mathcal{C}_{\text{max}}(\theta; V) &= \mathcal{Q}(\theta; \rho'_{\text{out}}[V]) \\ &\geq \mathcal{Q}(\theta; \sum_x |\zeta_x\rangle \langle \zeta_x|) \\ &= \mathcal{Q}\left(\theta; \frac{1}{1-N} \sum_m |r_m|^2 |\phi_m^S\rangle \langle \phi_m^S|\right) \\ &= \mathcal{Q}(\theta; \text{Tr}_I |\Phi_{\text{biph,out}}\rangle), \end{aligned} \quad (51)$$

where the first line is true because maximisation of the CFI over $\{\Pi_{y|x=x_m}^S\}$ in Eq. (43) is precisely the maximisation that yields the Cramér-Rao bound [33, 34] for the conditional state $\rho'_{\text{out}}[V]$ (see Eq. (D1) Appendix D). The second line is a consequence of the extended convexity of the QFI [70]. The inequality is saturated iff $\langle \phi_m^S | \partial_{\theta} \phi_n^S \rangle = 0 \forall m, n$. For a Schmidt basis $\{|\phi_n^S\rangle\}$ that is complete on the signal Hilbert space, this is never true, and we get the stronger inequality

$$\mathcal{C}_{\text{max}}(\theta; V) > \mathcal{Q}(\theta; \text{Tr}_I |\Phi_{\text{biph,out}}\rangle). \quad (52)$$

This shows that *all* measurement-optimal 1-LOCC detection schemes yield higher CFI than the QFI in signal photon obtained by tracing out the idler. Consequently, all measurement-optimal 1-LOCC detection schemes have a guaranteed metrological advantage over signal photon-only strategies. This leads to the hierarchy

$$\begin{aligned} \mathcal{Q}(\theta; |\Phi_{\text{biph,out}}\rangle) &= \mathcal{C}_{\text{max}}(\theta; V_{\text{opt}}) \geq \mathcal{C}_{\text{max}}(\theta; V) \\ &> \mathcal{Q}(\theta; \text{Tr}_I |\Phi_{\text{biph,out}}\rangle). \end{aligned} \quad (53)$$

D. Parameter-Independent Unitary $V = \mathbb{1}^I$

Unlike $V = V_{\text{opt}}$, $V = \mathbb{1}^I$ is independent of θ and $\{\phi_n^S\}$, and presents a simpler experimental scenario. The corresponding CFI is

$$\mathcal{C}_{\text{max}}(\theta; V = \mathbb{1}^I) = \quad (54)$$

$$\frac{4}{1-N} \sum_n |r_n|^2 \langle \partial_{\theta} \phi_n^S | \phi_n^S \rangle - \frac{4}{(1-N)^2} \sum_n |r_n|^2 \langle \phi_n^S | \phi_n^S \rangle^2.$$

For the special case of resonant Γ -estimation in a TLS with transition frequency ω_0 , it has been shown that [13, Section V A)]

$$\mathcal{Q}(\Gamma; |\Phi_{\text{biph,out}}\rangle)|_{\Delta=0} = \mathcal{C}_{\text{max}}(\Gamma; V = \mathbb{1}^I); \quad \Delta = \omega_0 - \bar{\omega}_S. \quad (55)$$

This implies that a 1-LOCC detection scheme with $V = \mathbb{1}^I$ attains the QFI for Γ -estimation at $\Delta = 0$ in a TLS. While this conclusion no longer holds for the spectroscopy of more general systems and parameters, the measurement-optimal $V = \mathbb{1}^I$ 1-LOCC detection scheme continues to be an improvement over simply tracing out the idler in the outgoing wavefunction, as per Eq. (53). We study its efficacy in spectroscopy with a PDC input probe numerically in Section VI.

VI. SPECTROSCOPY USING PDC LIGHT

We now study pulsed quantum light spectroscopy using the experimentally ubiquitous entangled probes of weakly-downconverted PDC states [13, Appendix H]

$$|\Phi_{\text{PDC}}\rangle \approx \frac{1}{N_{\text{PDC}}^{1/2}} \left(|0\rangle + \sum_{n=0}^{\infty} r_{n,\text{PDC}} |h_n^{\text{S}}\rangle |h_n^{\text{I}}\rangle \right), \quad (56)$$

where $|h_n^{\text{S}}\rangle$ and $|h_n^{\text{I}}\rangle$ are n -th Hermite-Gauss Schmidt basis modes for signal and idler spaces respectively, and $r_{n,\text{PDC}}$ are corresponding Schmidt weights. The JTA function for the incoming PDC states may be obtained by inverting Eq. (20) and recombining the Schmidt terms $\Phi_{\text{PDC}}(t_{\text{S}}, t_{\text{I}}) = \sum_n r_{n,\text{PDC}} h_n(t_{\text{S}}) h_n(t_{\text{I}})$. The time-frequency entanglement of PDC states can be quantified using the entanglement entropy function

$$S = - \sum_n |r_{n,\text{PDC}}|^2 \log |r_{n,\text{PDC}}|^2, \quad (57)$$

which is plotted as a function of PDC characteristics of entanglement time T_{qent} and pumpwidth σ_{p} (see [13, Appendix H] for definitions) in Figure 4.

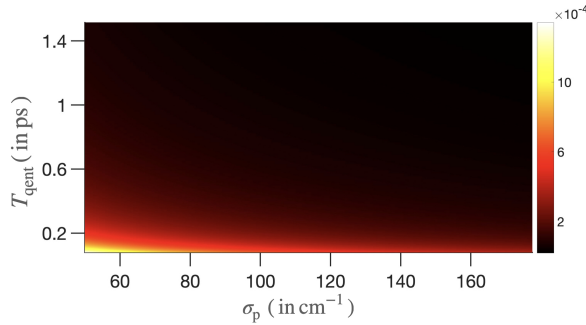


Figure 4. Plot of entanglement entropy S in Eq. (57) for PDC source characteristics - pump bandwidth (σ_{p}) and entanglement time (T_{qent}). The time-frequency entanglement is higher for short T_{qent} , and small values of σ_{p} . See [13, Appendix H] for definitions.

We show that for these most practical of entangled probes, time-frequency entanglement provides a functional advantage in biphoton spectroscopy for asymptotically long detection times. We also establish that it is possible to get close to the fundamental limits set by the corresponding QCRB using unentangled measurements that are independent of the true value of the parameter. We thus provide a complete recipe for quantum-enhanced biphoton spectroscopy using PDC light probes and simple, unentangled measurements independent of the sample parameters.

A. QFI Of Outgoing PDC State

The outgoing S-I state for the PDC input in Eq. (56) has a structure similar to Eq. (32), but with a modified

normalisation

$$\rho_{\text{PDC,out}}^{\text{SI}} = (1 - \mathbf{n}) |\Phi_{\text{PDC,out}}\rangle \langle \Phi_{\text{PDC,out}}| + \mathbf{n} |0^{\text{S}}\rangle \langle 0^{\text{S}}| \otimes \sigma^{\text{I}}, \quad (58)$$

where σ^{I} is the same as in Eq. (34), $\mathbf{n} = N/N_{\text{PDC}}$,

$$|\Phi_{\text{PDC,out}}\rangle = \frac{1}{(N_{\text{PDC}}(1 - \mathbf{n}))^{1/2}} \left(|0\rangle + \sum_n r_{n,\text{PDC}} |\phi_{n,\text{PDC}}^{\text{S}}\rangle |h_n^{\text{I}}\rangle \right), \quad (59)$$

with

$$|\phi_{n,\text{PDC}}^{\text{S}}\rangle = \int_{-\infty}^{\infty} dt_{\text{S}} \left(h_n(t_{\text{S}}) - \Gamma \int_{-\infty}^{t_{\text{S}}} d\tau f_{\text{M}}(t_{\text{S}} - \tau) h_n(t_{\text{S}}) \right) a_{\text{S}}^{\dagger}(t_{\text{S}}) |0^{\text{S}}\rangle. \quad (60)$$

The QFI of the outgoing PDC state has the familiar trinal contribution (cf. Eq. (37))

$$\mathcal{Q}(\theta; \rho_{\text{PDC,out}}^{\text{SI}}) = \mathcal{C}(\mathbf{n}, 1 - \mathbf{n}) + \mathbf{n} \mathcal{Q}(\theta; \sigma^{\text{I}}) + (1 - \mathbf{n}) \mathcal{Q}(\theta; |\Phi_{\text{PDC,out}}\rangle) \quad (61)$$

where

$$\mathcal{Q}(\theta; |\Phi_{\text{PDC,out}}\rangle) = \frac{4}{N_{\text{PDC}}(1 - \mathbf{n})} \sum_n |r_{n,\text{PDC}}|^2 \langle \partial_{\theta} \phi_{n,\text{PDC}}^{\text{S}} | \partial_{\theta} \phi_{n,\text{PDC}}^{\text{S}} \rangle - \frac{4}{(N_{\text{PDC}}(1 - \mathbf{n}))^2} \left| \sum_n |r_{n,\text{PDC}}|^2 \langle \phi_{n,\text{PDC}}^{\text{S}} | \partial_{\theta} \phi_{n,\text{PDC}}^{\text{S}} \rangle \right|^2. \quad (62)$$

The relative magnitudes of the three terms in the PDC QFI in Eq. (61) admit the same pattern with respect to the ratio Γ_{\perp}/Γ as established for the biphoton QFI in Table I, with the only modification being that all the Fisher informations in Eq. (62) are scaled by the Γ_{\perp}/Γ -independent normalisation N_{PDC} .

Also of interest is the CFI of the measurement-optimal 1-LOCC mediated by preparation step unitary $V = \mathbb{1}^{\text{I}}$ for the PDC states (see Eq. (54))

$$\mathcal{C}_{\text{max}}(\theta; V = \mathbb{1}^{\text{I}}) = \frac{4}{N_{\text{PDC}}(1 - \mathbf{n})} \sum_n |r_{n,\text{PDC}}|^2 \langle \partial_{\theta} \phi_{n,\text{PDC}}^{\text{S}} | \partial_{\theta} \phi_{n,\text{PDC}}^{\text{S}} \rangle - \frac{4}{(N_{\text{PDC}}(1 - \mathbf{n}))^2} \sum_n |r_{n,\text{PDC}}|^2 \left| \langle \phi_{n,\text{PDC}}^{\text{S}} | \partial_{\theta} \phi_{n,\text{PDC}}^{\text{S}} \rangle \right|^2. \quad (63)$$

Finally, some descriptions of the entangled PDC photons omit the vacuum term in Eq. (56), yielding just the biphoton state $|\Phi_{\text{biph}}\rangle$ in Eq. (19). This corresponds to the state post-selected for only successful detection of the two photons, and can be expressed in terms of the PDC JTA $\Phi_{\text{PDC}}(t_{\text{S}}, t_{\text{I}})$ as

$$|\Phi_{\text{biph}}\rangle = \frac{1}{\sqrt{\Lambda}} \int dt_{\text{S}} \int dt_{\text{I}} \Phi_{\text{PDC}}(t_{\text{S}}, t_{\text{I}}) a_{\text{S}}^{\dagger}(t_{\text{S}}) a_{\text{I}}^{\dagger}(t_{\text{I}}) |0\rangle, \quad (64)$$

where $\Lambda = \int dt_S \int dt_I \Phi_{\text{PDC}}^*(t_S, t_I) \Phi_{\text{PDC}}(t_S, t_I)$ ensures unit norm. The spectroscopic informations provided by states in Eqs. (56) and (64) are not, in general, a simple rescaling. Rather,

$$\begin{aligned} \mathcal{Q}(\theta; |\Phi_{\text{PDC},\text{out}}\rangle) &\approx \Lambda \mathcal{Q}(\theta; |\Phi_{\text{biph},\text{out}}\rangle) \\ &+ \frac{4}{\Lambda} \left| \int dt_S \int dt_I \partial_\theta \Phi_{\text{PDC},\text{out}}(t_S, t_I)^* \Phi_{\text{PDC},\text{out}}(t_S, t_I) \right|^2, \end{aligned} \quad (65)$$

assuming $N_{\text{PDC}} \approx 1$ and $\Lambda \ll 1$. See Appendix I for details.

We finally specialise our study of entangled quantum light spectroscopy to specific matter systems: in Section VIB, we address 1-site TLS ($P = 1$ in Eq. (11)) for which we will evaluate Fisher informations corresponding to pulse-matter coupling Γ , as well as level frequency ω_0 ; in Section VIC, we address the 2-site CD systems ($P = 2$ in Eq. (11)), for which we will evaluate fundamental limits of inter-site coupling J estimation. As a first foray, we focus on the vibrationless Hamiltonian that does not include couplings to phonon baths.

We highlight aspects of engineering the source of PDC probes for spectroscopy while yielding tangible quantum enhancements. We find larger time-frequency entanglement — concomitantly shorter entanglement times and pump bandwidths — to be beneficial. Indeed, more entanglement in the PDC probe yields more spectroscopic information. Parameter-independent (hence non-adaptive) unentangled detection, using the most entangled of PDC probes, also meaningfully outperform single-photon spectroscopies using the reduced signal state only. Typically, these simplified measurements capture between 60% - 90% of the spectroscopic information.

B. TLS spectroscopy

For the TLS, $H_I^M = \hbar\Delta|e\rangle\langle e|$, $\Delta = \omega_0 - \bar{\omega}_S$ is the detuning between the carrier signal and TLS frequency ω_0 , and the characteristic response function for TLS takes the simple form

$$f_{\text{TLS}}(t) = \exp\left(-\left[\frac{\Gamma + \Gamma_\perp}{2} + i\Delta\right]t\right). \quad (66)$$

1. No Coupling to Environment (E): $\Gamma_\perp = 0$

In this case, only the last term in Eq. (61) contributes. This QFI is plotted, for a grid of values of classical pumpwidths σ_p and entanglement times T_{qent} , for the estimation of Γ in Figure 5 (a), and for the ω_0 -parameter in Figure 5 (b). For both parameters, comparing Figs. 4 and 5 shows that more entanglement in the incoming PDC probe, as captured by entropy S defined in Eq. (57), leads to a higher value for the outgoing QFI.

To uncover the role of entanglement in the incoming probe PDC state in this spectroscopy task more clearly,

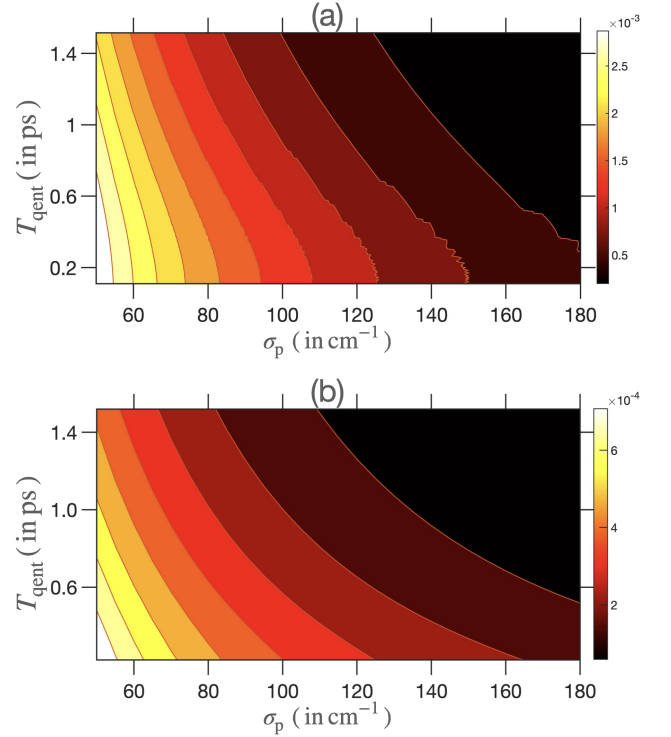


Figure 5. QFI $\mathcal{Q}(\theta; |\Phi_{\text{PDC},\text{out}}\rangle)$, calculated numerically using Eq. (62), for varying PDC entanglement time T_{qent} , and classical pumpwidth σ_p , for TLS parameters (a) $\theta \equiv \Gamma$, and (b) $\theta \equiv \omega_0$, and $\Gamma_\perp = 0$. ($\Gamma = 0.15$ THz, $\Delta = 0$ THz).

we also display scatter plots of the Γ - and ω_0 -QFIs as functions of the entanglement entropy S in Appendix E (see Figure 14 (a)-(b)). These show that that a more entangled PDC input always yields more outgoing QFI. However, the outgoing PDC QFI is not a one-to-one function of the incoming entanglement. Specifically, for the same amount of entanglement, incoming PDC states may yield outgoing states with different QFIs, depending on the experimental values of T_{qent} and σ_p .

The apparent advantage conferred by time-frequency entanglement here is not in contradiction with our earlier conclusion that entanglement provides no in-principle advantage in biphoton spectroscopy. In Section VB we showed that the outgoing QFI corresponding to *any* incoming entangled state may be superseded by a suitably optimised product state in the S-I space. In contrast, entanglement-enhanced sensing in Figure 5 is relative to PDC probe states *only*.

For reference, in Figure 5, the ratios of outgoing QFI corresponding to the most entangled PDC state (bottom-left edge in either plot) to that of the least entangled (almost product) PDC state (top-right edge) are

$$\frac{\mathcal{Q}(\Gamma; |\Phi_{\text{PDC},\text{out}}\rangle)|_{T_{\text{qent}}=0.150 \text{ ps}, \sigma_p=50 \text{ cm}^{-1}}}{\mathcal{Q}(\Gamma; |\Phi_{\text{PDC},\text{out}}\rangle)|_{T_{\text{qent}}=1.995 \text{ ps}, \sigma_p=180 \text{ cm}^{-1}}} \approx 14.0391, \quad (67)$$

and

$$\frac{\mathcal{Q}(\omega_0; |\Phi_{\text{PDC,out}}\rangle)|_{T_{\text{qent}}=0.150 \text{ ps}, \sigma_p=50 \text{ cm}^{-1}}}{\mathcal{Q}(\omega_0; |\Phi_{\text{PDC,out}}\rangle)|_{T_{\text{qent}}=1.995 \text{ ps}, \sigma_p=180 \text{ cm}^{-1}}} \approx 15.5665, \quad (68)$$

showing that for TLS spectroscopy, there is significant advantage to engineering the source to produce more entangled states — within the class of PDC states. Our result also indicates that, for the parameter regime considered, using entangled photons enables more precise spectroscopy than heralded single photon states [71–73].

To further underscore the subtle role of entanglement, we consider a family of time-frequency pulse mode (TFM) states of the form [74]

$$|\Phi_{\text{TFM}}\rangle = \frac{1}{N_{\text{TFM}}^{1/2}} \left(|0\rangle + \frac{\alpha_{\text{pump}}}{\hbar} |\Phi_{\text{TFM}}^t\rangle \right), \quad (69)$$

where

$$|\Phi_{\text{TFM}}^t\rangle = \cos t |h_0^S\rangle |h_1^I\rangle + \sin t |h_1^S\rangle |h_0^I\rangle, \quad 0 \leq t \leq \pi, \quad (70)$$

and $\alpha_{\text{pump}}/\hbar = 0.01$ (same as for $|\Phi_{\text{PDC}}\rangle$). Parametric plots of the QFI of the outgoing TFM state against the entanglement of the incoming state in Figure 15 in Appendix E show that for both TLS parameters, the maximal QFI in outgoing state corresponds to the product input $|h_0^S\rangle |h_1^I\rangle$. Thus, for this family of biphoton states, time-frequency mode entanglement is not a useful resource.

As a final caveat, recall that our conclusions are for asymptotically large times. They may not hold in general for finite-time evolutions. As a matter of fact, an opposite behaviour was shown in a similar parameter region [13] for short detection times, where the problem essentially reduces to absorption estimation, and the perturbation induced on the signal photon wavefunction is not relevant. This further highlights the intricacies in understanding the role of entanglement in quantum light spectroscopy.

To understand the measurements that attain a large fraction of the maximal spectroscopic information, we now define two ratios to capture the efficacy of $\mathcal{C}_{\text{max}}(\theta; V = \mathbb{1}^I)$. They are motivated by the simpler parameter-independent $V = \mathbb{1}^I$ measurements enabling practical entangled light spectroscopy. The first is a “degree of optimality” defined as

$$\varkappa(\theta) = \frac{\mathcal{C}_{\text{max}}(\theta; V = \mathbb{1}^I)}{\mathcal{Q}(\theta; |\Phi_{\text{PDC,out}}\rangle)}, \quad 0 \leq \varkappa(\theta) \leq 1. \quad (71)$$

A value closer to unity indicates proximity to the fundamental precision afforded by appropriately constructed estimators set by the PDC QFI, which for $\Gamma_{\perp} = 0$ is the biphoton QFI $\mathcal{Q}(\theta; |\Phi_{\text{PDC,out}}(\theta)\rangle)$ only.

The second is an “enhancement factor” defined as

$$\varsigma(\theta) = \frac{\mathcal{C}_{\text{max}}(\theta; V = \mathbb{1}^I)}{\mathcal{Q}(\theta; \text{Tr}_I[|\Phi_{\text{PDC,out}}\rangle])}, \quad \varsigma(\theta) > 1, \quad (72)$$

where $\varsigma(\theta) > 1$ indicates a spectroscopic advantage offered by 1-LOCC measurement with $V = \mathbb{1}^I$ over all

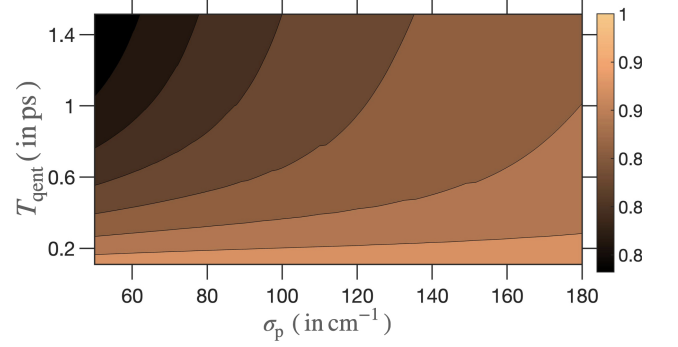


Figure 6. Degree of optimality as per the ratio $\varkappa(\omega_0)$ using PDC light, for $\Gamma = 0.15$ THz, $\Delta = 0$ THz.

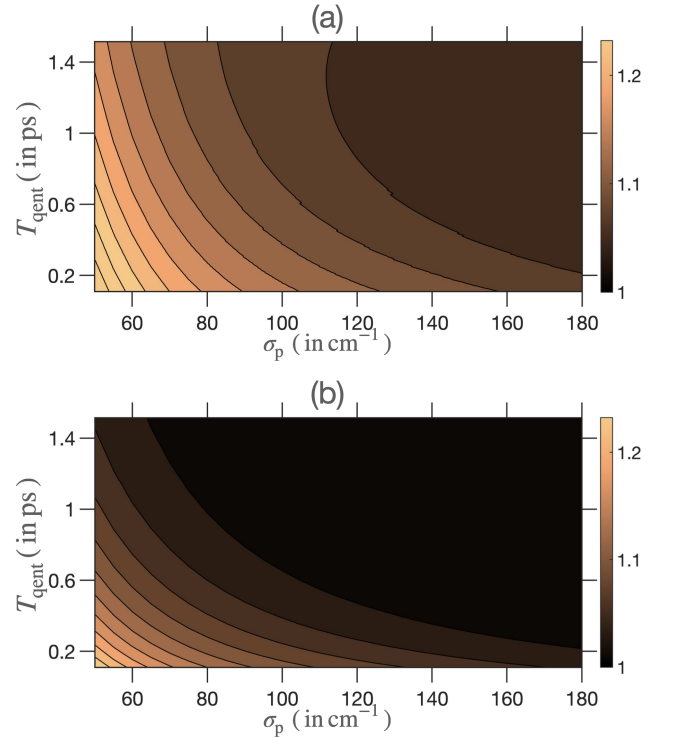


Figure 7. Enhancement factor $\varsigma(\theta)$ for estimation of TLS parameters (a) Γ , and (b) ω_0 using PDC light, for $\Gamma = 0.15$ THz, $\Delta = 0$ THz.

single-photon strategies on the reduced signal-photon state $\text{Tr}_I[|\Phi_{\text{PDC,out}}\rangle]$. For completeness,

$$\mathcal{Q}(\theta; \text{Tr}_I[|\Phi_{\text{PDC,out}}\rangle]) = \mathcal{C}_{\text{max}}(\theta; V = \mathbb{1}^I) - \frac{1}{(N_{\text{PDC}}(1 - \mathbf{n}))^2} \sum_{n>m} \frac{16 |r_m|^2 |r_n|^2}{|r_m|^2 + |r_n|^2} |\langle \phi_{m,\text{PDC}}^S | \partial_\theta \phi_{n,\text{PDC}}^S \rangle|^2. \quad (73)$$

Figure 6 displays the optimality ratio $\varkappa(\theta)$ for the TLS parameter ω_0 when $\Delta = 0$. It shows that more than 80% of the QFI for a PDC probe is recovered by a parameter-independent 1-LOCC measurement. For resonant Γ estimation, $\varkappa(\Gamma)|_{\Delta=0} = 1$ for all points on the

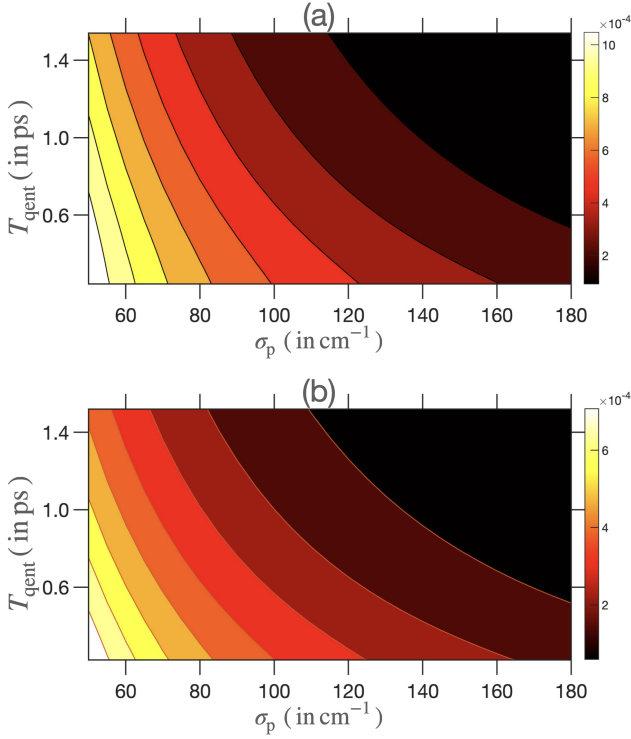


Figure 8. QFI $\mathcal{Q}(\Gamma; |\Phi_{\text{PDC,out}}\rangle)$ for varying PDC entanglement time T_{qent} , and classical pumpwidth σ_p , for TLS parameter Γ , and free space M-E coupling set to (a) $\Gamma_{\perp}/\Gamma = 0.5$, and (b) $\Gamma_{\perp}/\Gamma = 10.0$. Note the change in scale of QFI values between the two plots. ($\Gamma = 0.15$ THz, $\Delta = 0$ THz).

grid [13]. As the magnitude of the detuning $|\Delta|$ increases, $\langle \Phi_{\text{PDC,out}} | \partial_{\Gamma} \Phi_{\text{PDC,out}} \rangle_{|\Delta \neq 0} \neq 0$, and the degree of optimality drops below unity, as can be seen in Figure 18 in Appendix F.

Lastly, Figure 7 displays the enhancement factor $\zeta(\theta)$ for TLS parameters ω_0 and Γ . From Eq. (52), we always expect $\zeta(\theta) > 1$, which is substantiated in these plots. We also see that spectroscopy with only the most entangled of PDC states can meaningfully outperform single-photon spectroscopy using the reduced signal state $\text{Tr}_I[|\Phi_{\text{PDC,out}}\rangle]$. Interestingly, for ω_0 -estimation, a more entangled state yields a larger $\zeta(\omega_0)$ as the detuning $|\Delta|$ increases, whereas the reverse is true for $\zeta(\Gamma)$. For the effects of non-zero $|\Delta|$ on these quantities, see Appendix F. This has practical consequences for spectroscopy using PDC probes, as one may resort to the even simpler setup of single photon probes if the enhancement offered by the 1-LOCC scheme, as measured by $\zeta(\theta)$ is not large enough.

2. Coupling to Environment (E): $\Gamma_{\perp} > 0$

For non-zero coupling to the environmental modes in E so that $\Gamma_{\perp} > 0$, the outgoing two-photon QFI must now be evaluated using Eq. (61) which includes contributions from both single- and two-photon terms, in addition to the

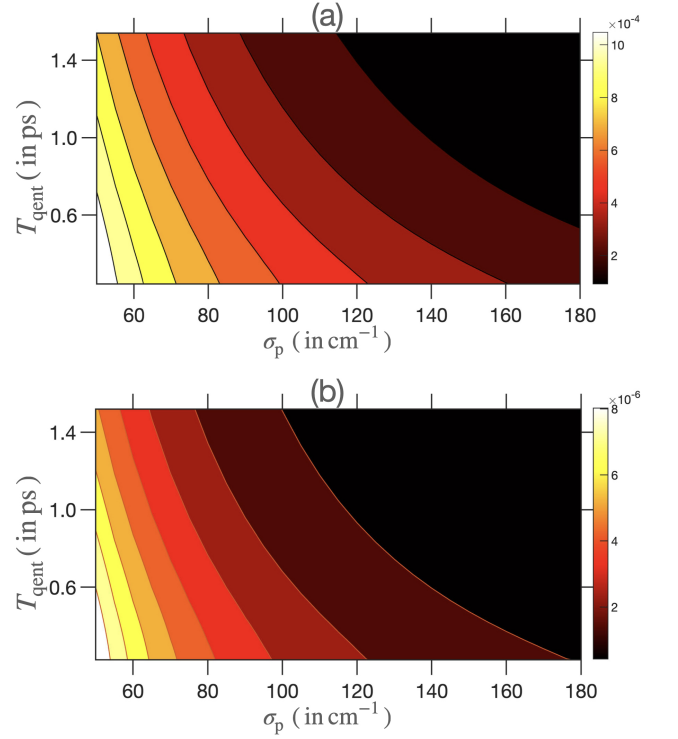


Figure 9. QFI $\mathcal{Q}(\omega_0; |\Phi_{\text{PDC,out}}\rangle)$ for varying PDC entanglement time T_{qent} , and classical pumpwidth σ_p , for TLS parameter ω_0 , and free space M-E coupling set to (a) $\Gamma_{\perp}/\Gamma = 0.5$, and (b) $\Gamma_{\perp}/\Gamma = 10.0$. Note the change in scale of QFI values between the two plots. ($\Gamma = 0.15$ THz, $\Delta = 0$ THz).

term corresponding to classical mixing. Figure 8 displays the outgoing Γ -QFI (for the same grid of values as Figure 5 and $\Delta = 0$) for two representative values of M-E coupling. In panel (a), $\Gamma_{\perp} = 0.5\Gamma$ corresponds to comparable M-S and M-E couplings, whereas panel (b) corresponds to $\Gamma_{\perp} = 10.0\Gamma$ such that the matter-environment coupling is much stronger than coupling to the incoming signal mode. Corresponding results are shown in Figure 9 for ω_0 -QFI. The effect of non-zero detuning on TLS parameter QFIs in the presence of an environment is studied in Appendix F.

Even in the presence of an environment, Figures 8 and 9 show that time-frequency entanglement continues to be a useful resource for spectroscopy using PDC probes. The magnitudes of the QFI values for either TLS parameter are also diminished, an expected consequence of the M-E coupling which causes the matter sample to decay into the environmental modes, thus reducing the information content in the measured signal and idler modes.

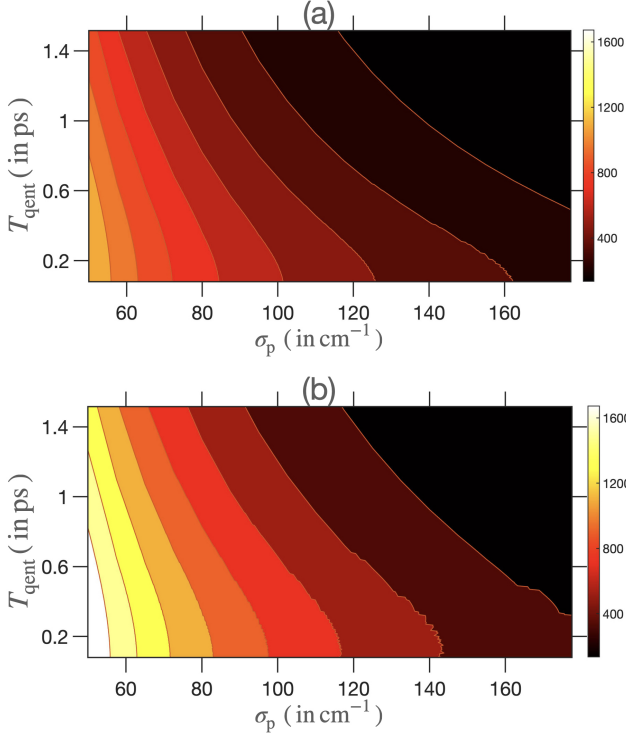


Figure 10. QFI $\mathcal{Q}(J; |\Phi_{\text{PDC,out}}\rangle)$ for varying PDC entanglement time T_{qent} , and classical pumpwidth σ_p , for CD interstitial coupling J , and (a) $\bar{\omega}_S = \omega_\alpha$, and (b) $\bar{\omega}_S = \omega_\beta$. The CD parameters used are those of the allophycocyanin dimer [20] — $\hbar\omega_a = 1.6$ eV, $\hbar\omega_b = 1.8$ eV, $J = -0.07$ eV, $\mu_a = 1$ Debye and $\mu_b = 1.5$ Debye. ($\Gamma = 0.15$ THz)

C. CD spectroscopy: J -estimation

The Hamiltonian of a coupled dimer (CD) ($P = 2$ in Eq. (11)) is given by

$$H^{\text{CD}} = \sum_{j=a,b} \hbar\omega_j |j\rangle\langle j| + \hbar(\omega_a + \omega_b) |f\rangle\langle f| + J(|a\rangle\langle b| + |b\rangle\langle a|), \quad (74)$$

where J is the coupling strength between the two sites a and b (see Figure 1). Transforming to an appropriately chosen interaction frame and diagonalising the matter-only part (details in Appendix G), we can express the CD Hamiltonian in the delocalised excitonic basis as

$$H_I^{\text{CD}} = \sum_{i=\alpha,\beta} \hbar\Delta_i |i\rangle\langle i| + \hbar(\Delta_\alpha + \Delta_\beta) |f\rangle\langle f|, \quad (75)$$

where $\Delta_i = \omega_i - \bar{\omega}_S$ ($i = \alpha, \beta$) are the detunings from the central signal pulse frequency of the singly-excited manifold (SEM) excitonic levels $|\alpha\rangle$ and $|\beta\rangle$.

The explicit form for the characteristic CD function $f_{\text{CD}}(t)$ appears in Appendix H. It can be used to evaluate (assuming no M-E coupling so that $\Gamma_\perp = 0$) the fundamental limits on the J coupling parameter between the sites a and b , using Eq. (61).

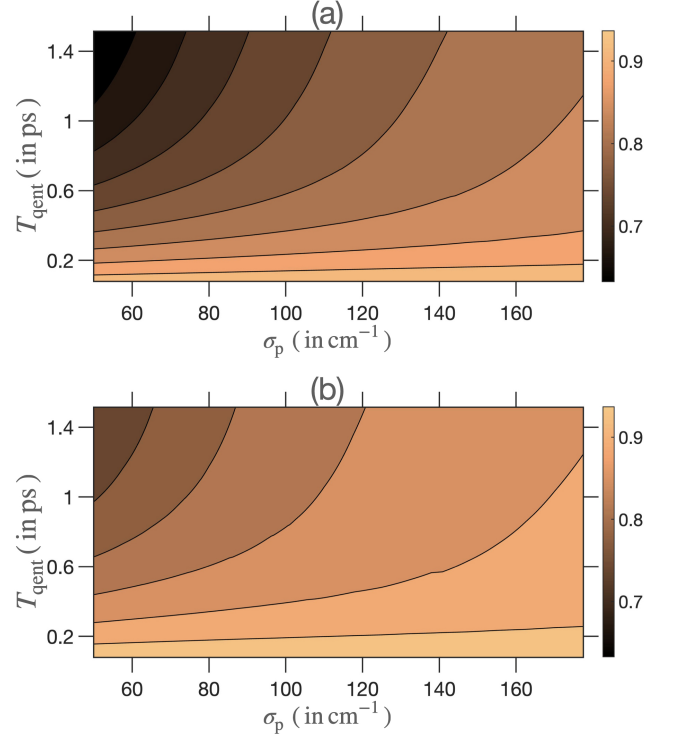


Figure 11. Degree of optimality $\varkappa(J)$ for estimation of CD parameter J , with (a) $\bar{\omega}_S = \omega_\alpha$, and (b) $\bar{\omega}_S = \omega_\beta$ using PDC light, for $\Gamma = 0.15$ THz, $\Delta = 0$ THz.

In Figure 10, the J -QFI are plotted as heat maps, for identical ranges of σ_p and T_{qent} values as for entanglement entropy S in Figure 4, for signal carrier frequency $\bar{\omega}_S$ resonant with ω_α in panel (a), and ω_β in panel (b). Akin to TLS estimation, we find that a higher value of the entanglement entropy of the incoming PDC state, for the parameter ranges considered, yields a higher J -QFI. (see Figure 14 (c)-(d) in Appendix E for parametric $\mathcal{Q}(J; |\Phi_{\text{PDC,out}}\rangle) - S$ plots.) This implies again that, within the set of PDC probes, more time-frequency entanglement enhances the spectroscopic performance of J -estimation.

We also see that the values of J -QFI for $\bar{\omega}_S = \omega_\alpha$ (so that the signal beam is resonant with the g - α transition) are smaller than that for the choice $\bar{\omega}_S = \omega_\beta$ (signal beam resonant with g - β transition). This can be attributed to our choice of the small absolute value of $|\hbar(\omega_a - \omega_b)|$ relative to $\hbar\omega_a$ and $\hbar\omega_b$, meaning that the particular instance of the CD system that we are studying, for which $2|\omega_a - \omega_b|/(\omega_a + \omega_b) \approx 0.11$, is quite close to a homodimer for which the g - α transition is forbidden by the structure of the GSM-SEM dipole operator. Therefore, population transfer from $|g\rangle \rightarrow |\alpha\rangle$ for $\bar{\omega}_S = \omega_\alpha$ is much smaller than for $|g\rangle \rightarrow |\beta\rangle$ when $\bar{\omega}_S = \omega_\beta$, which accounts for the smaller values of the J -QFI.

Next, Figure 11 displays the ratio $\varkappa(J)$ that captures the degree of optimality of the $V = \mathbf{1}^I$ measurement-optimal idler-to-signal scheme. For the central signal

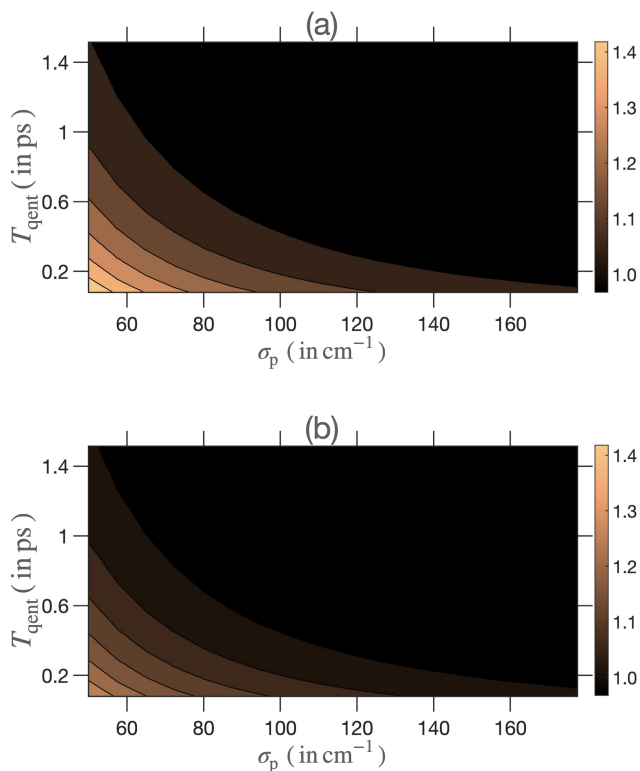


Figure 12. Enhancement factor $\zeta(J)$ for CD parameter J , with (a) $\bar{\omega}_S = \omega_\alpha$, and (b) $\bar{\omega}_S = \omega_\beta$ using PDC light, for $\Gamma = 0.15$ THz, $\Delta = 0$ THz.

frequency $\bar{\omega}_S$ set to either ω_α or ω_β , we see that the $V = \mathbb{1}^I$ idler-to-signal LOCC scheme recovers between 60%-90% of the QFI, especially for highly entangled states in the the bottom right corner.

Finally, Figure 12 displays the enhancement factor $\zeta(J)$. For all values on the grid except for most highly entangled states with small values of σ_p and T_{qent} , $\zeta(J)$ is close to unity. As for TLS spectroscopy, CD spectroscopy with only the most entangled of PDC states can meaningfully outperform single-photon spectroscopy using the reduced state of the signal photon only, $\text{Tr}_I[|\Phi_{\text{PDC,out}}\rangle]$.

VII. CONCLUSIONS

Our quantum-information theoretic analysis of single-molecule biphoton spectroscopy of arbitrary quantum

systems provides a characterisation of all the spectroscopic information that exists and can, in principle, be extracted using a biphoton probe in the long-time regime, when the excitation induced by the input pulse in the matter system has decayed. This allows the design of simple unentangled measurements that can provide tangible quantum advantage in practice.

We provide a detailed analysis of the theoretical and experimental utility of time-frequency entanglement in single-molecule biphoton spectroscopy. With the latter in mind, we compare the performance of biphoton spectroscopy to those with unentangled probes, especially single photons, and unentangled measurements. This reveals the subtle and intricate role entanglement can play in enhancing spectroscopic performance.

Note added: A recent work [75] examined the usefulness of quantum entangled light vis-à-vis classical coherent pulses in a non-linear generalisation of the biphoton setup in Figure 1. It focuses on the absorption signal (hence small detection times) for ensemble systems, whereas we study fundamental limits of spectroscopic information for coherent single-molecule spectroscopies and asymptotically long detection times.

ACKNOWLEDGMENTS

We thank Elnaz Darsheshdar and Sourav Das for fruitful discussions and feedback on the manuscript. This work has been funded, in part, by an EPSRC New Horizons grant (EP/V04818X/1) and the UKRI (Reference Number: 10038209) under the UK Government's Horizon Europe Guarantee for the Research and Innovation Programme under agreement 101070700. AK was supported, in part, by a Chancellor's International Scholarship from the University of Warwick. Computing facilities were provided by the Scientific Computing Research Technology Platform of the University of Warwick.

-
- [1] A. Stefanov, On the role of entanglement in two-photon metrology, *Quantum science and technology* **2**, 025004 (2017).
 [2] A. Yabushita and T. Kobayashi, Spectroscopy by frequency-entangled photon pairs, *Physical Review A* **69**, 013806 (2004).
 [3] A. Kalachev, D. Kalashnikov, A. Kalinkin, T. Mitrofanova,

- A. Shkalikov, and V. Samartsev, Biphoton spectroscopy of yag: Er3+ crystal, *Laser Physics Letters* **4**, 722 (2007).
 [4] D. A. Kalashnikov, Z. Pan, A. I. Kuznetsov, and L. A. Krivitsky, Quantum spectroscopy of plasmonic nanostructures, *Physical Review X* **4**, 011049 (2014).
 [5] K. E. Dorfman, F. Schlawin, and S. Mukamel, Nonlinear optical signals and spectroscopy with quantum light,

- Reviews of Modern Physics* **88**, 045008 (2016).
- [6] F. Schlawin, Entangled photon spectroscopy, *Journal of Physics B: Atomic, Molecular and Optical Physics* **50**, 203001 (2017).
 - [7] F. Schlawin, K. E. Dorfman, and S. Mukamel, Entangled two-photon absorption spectroscopy, *Accounts of chemical research* **51**, 2207 (2018).
 - [8] S. Mukamel, M. Freyberger, W. Schleich, M. Bellini, A. Zavatta, G. Leuchs, C. Silberhorn, R. W. Boyd, L. L. Sánchez-Soto, A. Stefanov, *et al.*, Roadmap on quantum light spectroscopy, *Journal of Physics B: Atomic, Molecular and Optical Physics* **53**, 072002 (2020).
 - [9] M. G. Raymer, T. Landes, and A. H. Marcus, Entangled two-photon absorption by atoms and molecules: A quantum optics tutorial, *The Journal of Chemical Physics* **155**, 081501 (2021).
 - [10] K. M. Parzuchowski, A. Mikhaylov, M. D. Mazurek, R. N. Wilson, D. J. Lum, T. Gerrits, C. H. Camp, M. J. Stevens, and R. Jimenez, Setting bounds on entangled two-photon absorption cross sections in common fluorophores, *Physical Review Applied* **15**, 10.1103/physrevapplied.15.044012 (2021).
 - [11] S. Corona-Aquino, O. Calderón-Losada, M. Y. Li-Gómez, H. Cruz-Ramirez, V. Álvarez-Venicio, M. del Pilar Carreón-Castro, R. de J. León-Montiel, and A. B. U'Ren, Experimental study of the validity of entangled two-photon absorption measurements in organic compounds, *The Journal of Physical Chemistry A* **126**, 2185 (2022).
 - [12] B. E. Saleh, B. M. Jost, H.-B. Fei, and M. C. Teich, Entangled-photon virtual-state spectroscopy, *Physical review letters* **80**, 3483 (1998).
 - [13] F. Albarelli, E. Bisketzi, A. Khan, and A. Datta, Fundamental limits of pulsed quantum light spectroscopy: Dipole moment estimation, *Phys. Rev. A* **107**, 062601 (2023).
 - [14] E. Carnio, A. Buchleitner, and F. Schlawin, How to optimize the absorption of two entangled photons, *SciPost Physics Core* **4**, 028 (2021).
 - [15] Y. Fujihashi, K. Miwa, M. Higashi, and A. Ishizaki, Probing exciton dynamics with spectral selectivity through the use of quantum entangled photons, arXiv preprint arXiv:2212.11519 <https://doi.org/10.48550/arXiv.2212.11519> (2022).
 - [16] D. A. Steck, *Quantum and Atom Optics*, revision 0.13.12, 25 may 2022 ed. (2007).
 - [17] A. Ishizaki and G. R. Fleming, On the adequacy of the redfield equation and related approaches to the study of quantum dynamics in electronic energy transfer, *The Journal of chemical physics* **130**, 234110 (2009).
 - [18] M. Marcus, G. C. Knee, and A. Datta, Towards a spectroscopic protocol for unambiguous detection of quantum coherence in excitonic energy transport, *Faraday Discussions* **221**, 110 (2020).
 - [19] A. Khan, D. Quigley, M. Marcus, E. Thyryhaug, and A. Datta, Model-independent simulation complexity of complex quantum dynamics, *Physical Review Letters* **126**, 150402 (2021).
 - [20] J. M. Womick and A. M. Moran, Exciton coherence and energy transport in the light-harvesting dimers of allophycocyanin, *The Journal of Physical Chemistry B* **113**, 15747 (2009).
 - [21] W. Barford and O. R. Tozer, Theory of exciton transfer and diffusion in conjugated polymers, *The Journal of chemical physics* **141**, 164103 (2014).
 - [22] W. Barford, Exciton dynamics in conjugated polymer systems, *Frontiers in Physics* , 963 (2022).
 - [23] S. Chong, W. Min, and X. S. Xie, Ground-state depletion microscopy: detection sensitivity of single-molecule optical absorption at room temperature, *The journal of physical chemistry letters* **1**, 3316 (2010).
 - [24] M. Celebrano, P. Kukura, A. Renn, and V. Sandoghdar, Single-molecule imaging by optical absorption, *Nature Photonics* **5**, 95 (2011).
 - [25] E. M. van Dijk, J. Hernando, J.-J. García-López, M. Crego-Calama, D. N. Reinhoudt, L. Kuipers, M. F. García-Parajó, and N. F. van Hulst, Single-molecule pump-probe detection resolves ultrafast pathways in individual and coupled quantum systems, *Physical review letters* **94**, 078302 (2005).
 - [26] E. Van Dijk, J. Hernando, M. García-Parajó, and N. Van Hulst, Single-molecule pump-probe experiments reveal variations in ultrafast energy redistribution, *The Journal of chemical physics* **123**, 064703 (2005).
 - [27] R. Moya, A. C. Norris, T. Kondo, and G. S. Schlau-Cohen, Observation of robust energy transfer in the photosynthetic protein allophycocyanin using single-molecule pump-probe spectroscopy, *Nature Chemistry* **14**, 153 (2022).
 - [28] R. Nair, Quantum-limited loss sensing: Multiparameter estimation and bures distance between loss channels, *Physical Review Letters* **121**, 230801 (2018).
 - [29] H. T. Dinani, M. K. Gupta, J. P. Dowling, and D. W. Berry, Quantum-enhanced spectroscopy with entangled multiphoton states, *Physical Review A* **93**, 063804 (2016).
 - [30] H. Shi, Z. Zhang, S. Pirandola, and Q. Zhuang, Entanglement-assisted absorption spectroscopy, *Physical Review Letters* **125**, 180502 (2020).
 - [31] C. R. Rao, Information and the accuracy attainable in the estimation of statistical parameters, in *Breakthroughs in statistics* (Springer, 1992) pp. 235–247.
 - [32] H. Cramér, Mathematical methods of statistics (pms-9), volume 9, in *Mathematical Methods of Statistics (PMS-9), Volume 9* (Princeton university press, 2016).
 - [33] S. L. Braunstein and C. M. Caves, Statistical distance and the geometry of quantum states, *Physical Review Letters* **72**, 3439 (1994).
 - [34] M. G. Paris, Quantum estimation for quantum technology, *International Journal of Quantum Information* **7**, 125 (2009).
 - [35] S. Kurdzialek and R. Demkowicz-Dobrzański, Measurement noise susceptibility in quantum estimation, *Physical Review Letters* **130**, 160802 (2023).
 - [36] J. Liu, X.-X. Jing, W. Zhong, and X.-G. Wang, Quantum fisher information for density matrices with arbitrary ranks, *Communications in Theoretical Physics* **61**, 45 (2014).
 - [37] J. Liu, H. Yuan, X.-M. Lu, and X. Wang, Quantum fisher information matrix and multiparameter estimation, *Journal of Physics A: Mathematical and Theoretical* **53**, 023001 (2019).
 - [38] L. Mandel and E. Wolf, *Optical Coherence and Quantum Optics* (Cambridge University Press, 1995).
 - [39] K. Blow, R. Loudon, S. J. Phoenix, and T. Shepherd, Continuum fields in quantum optics, *Physical Review A* **42**, 4102 (1990).
 - [40] M. I. Kolobov, The spatial behavior of nonclassical light, *Reviews of Modern Physics* **71**, 1539 (1999).
 - [41] R. Loudon, *The Quantum Theory of Light* (OUP Oxford,

- 2000).
- [42] L. Ko, R. L. Cook, and K. B. Whaley, Dynamics of photosynthetic light harvesting systems interacting with n-photon fock states, *The Journal of Chemical Physics* **156**, 244108 (2022).
- [43] I. H. Deutsch and J. C. Garrison, Paraxial quantum propagation, *Physical Review A* **43**, 2498 (1991).
- [44] L. Lamata and J. León, Dealing with entanglement of continuous variables: Schmidt decomposition with discrete sets of orthogonal functions, *Journal of Optics B: Quantum and Semiclassical Optics* **7**, 224 (2005).
- [45] H. Takesue and K. Inoue, Generation of polarization-entangled photon pairs and violation of bell's inequality using spontaneous four-wave mixing in a fiber loop, *Physical Review A* **70**, 031802 (2004).
- [46] J. Chen, X. Li, and P. Kumar, Two-photon-state generation via four-wave mixing in optical fibers, *Physical Review A* **72**, 033801 (2005).
- [47] Q. Glorieux, J. B. Clark, N. V. Corzo, and P. D. Lett, Generation of pulsed bipartite entanglement using four-wave mixing, *New Journal of Physics* **14**, 123024 (2012).
- [48] W. Konyk and J. Gea-Banacloche, Quantum multimode treatment of light scattering by an atom in a waveguide, *Physical Review A* **93**, 063807 (2016).
- [49] N. Imoto, H. Haus, and Y. Yamamoto, Quantum non-demolition measurement of the photon number via the optical kerr effect, *Physical Review A* **32**, 2287 (1985).
- [50] W. Munro, K. Nemoto, R. Beausoleil, and T. Spiller, High-efficiency quantum-nondemolition single-photon-number-resolving detector, *Physical Review A* **71**, 033819 (2005).
- [51] C. C. Gerry and T. Bui, Quantum non-demolition measurement of photon number using weak nonlinearities, *Physics Letters A* **372**, 7101 (2008).
- [52] G. Nogues, A. Rauschenbeutel, S. Osnaghi, M. Brune, J.-M. Raimond, and S. Haroche, Seeing a single photon without destroying it, *Nature* **400**, 239 (1999).
- [53] C. Guerlin, J. Bernu, S. Deleglise, C. Sayrin, S. Gleyzes, S. Kuhr, M. Brune, J.-M. Raimond, and S. Haroche, Progressive field-state collapse and quantum non-demolition photon counting, *Nature* **448**, 889 (2007).
- [54] D. Malz and J. I. Cirac, Nondestructive photon counting in waveguide qed, *Physical Review Research* **2**, 033091 (2020).
- [55] A. Eckstein, B. Brecht, and C. Silberhorn, A quantum pulse gate based on spectrally engineered sum frequency generation, *Optics express* **19**, 13770 (2011).
- [56] J. M. Donohue, V. Ansari, J. Řeháček, Z. Hradil, B. Stoklasa, M. Pař, L. L. Sánchez-Soto, and C. Silberhorn, Quantum-limited time-frequency estimation through mode-selective photon measurement, *Physical review letters* **121**, 090501 (2018).
- [57] D. V. Reddy and M. G. Raymer, Photonic temporal-mode multiplexing by quantum frequency conversion in a dichroic-finesse cavity, *Optics Express* **26**, 28091 (2018).
- [58] S. De, J. Gil-Lopez, B. Brecht, C. Silberhorn, L. L. Sánchez-Soto, Z. Hradil, and J. Řeháček, Effects of coherence on temporal resolution, *Physical Review Research* **3**, 033082 (2021).
- [59] V. Ansari, B. Brecht, J. Gil-López, J. M. Donohue, J. Řeháček, Z. Hradil, L. L. Sánchez-Soto, and C. Silberhorn, Achieving the ultimate quantum timing resolution, *PRX Quantum* **2**, 010301 (2021).
- [60] M. Garikapati, S. Kumar, H. Zhang, Y. M. Sua, and Y.-P. Huang, A programmable spatiotemporal quantum parametric mode sorter, arXiv preprint arXiv:2210.16517 <https://arxiv.org/abs/2210.16517> (2022).
- [61] R. Horodecki, P. Horodecki, M. Horodecki, and K. Horodecki, Quantum entanglement, *Reviews of modern physics* **81**, 865 (2009).
- [62] S. Zhou, C.-L. Zou, and L. Jiang, Saturating the quantum cramer-rao bound using locc, *Quantum Science and Technology* **5**, 025005 (2020).
- [63] N. Friis, D. Orsucci, M. Skotiniotis, P. Sekatski, V. Dunjko, H. J. Briegel, and W. Dür, Flexible resources for quantum metrology, *New Journal of Physics* **19**, 063044 (2017).
- [64] N. Lee, H. Benichi, Y. Takeno, S. Takeda, J. Webb, E. Huntington, and A. Furusawa, Teleportation of non-classical wave packets of light, *Science* **332**, 330 (2011).
- [65] M. Huo, J. Qin, J. Cheng, Z. Yan, Z. Qin, X. Su, X. Jia, C. Xie, and K. Peng, Deterministic quantum teleportation through fiber channels, *Science advances* **4**, eaas9401 (2018).
- [66] Y. Chen, R. de J León-Montiel, and L. Chen, Quantum interferometric two-photon excitation spectroscopy, *New Journal of Physics* **24**, 113014 (2022).
- [67] S. Asban, V. Y. Chernyak, and S. Mukamel, Nonlinear quantum interferometric spectroscopy with entangled photon pairs, *The Journal of Chemical Physics* **156**, 094202 (2022).
- [68] S. Panahiyan, C. S. Muñoz, M. V. Chekhova, and F. Schlawin, Nonlinear interferometry for quantum-enhanced measurements of multiphoton absorption, *Physical Review Letters* **130**, 203604 (2023).
- [69] P. A. Fillmore, On similarity and the diagonal of a matrix, *The American Mathematical Monthly* **76**, 167 (1969).
- [70] S. Alipour and A. T. Rezakhani, Extended convexity of quantum fisher information in quantum metrology, *Physical Review A* **91**, 042104 (2015).
- [71] T. Pittman, B. Jacobs, and J. Franson, Heralding single photons from pulsed parametric down-conversion, *Optics communications* **246**, 545 (2005).
- [72] P. J. Mosley, J. S. Lundeen, B. J. Smith, P. Wasylczyk, A. B. U'Ren, C. Silberhorn, and I. A. Walmsley, Heralded generation of ultrafast single photons in pure quantum states, *Physical Review Letters* **100**, 133601 (2008).
- [73] F. Kaneda, K. Garay-Palmett, A. B. U'Ren, and P. G. Kwiat, Heralded single-photon source utilizing highly non-degenerate, spectrally factorable spontaneous parametric downconversion, *Optics express* **24**, 10733 (2016).
- [74] F. Graffitti, P. Barrow, A. Pickston, A. M. Brańczyk, and A. Fedrizzi, Direct generation of tailored pulse-mode entanglement, *Physical Review Letters* **124**, 053603 (2020).
- [75] L. Ko, R. L. Cook, and B. Whaley, Performing quantum entangled biphoton spectroscopy using classical light pulses, arXiv preprint arXiv:2306.14424 <https://doi.org/10.48550/arXiv.2306.14424> (2023).
- [76] M. Yang and G. R. Fleming, Influence of phonons on exciton transfer dynamics: comparison of the redfield, förster, and modified redfield equations, *Chemical physics* **282**, 163 (2002).
- [77] A. Ishizaki and G. R. Fleming, Unified treatment of quantum coherent and incoherent hopping dynamics in electronic energy transfer: Reduced hierarchy equation approach, *The Journal of chemical physics* **130**, 234111 (2009).
- [78] A. Ishizaki and G. R. Fleming, Theoretical examination of quantum coherence in a photosynthetic system at physiological temperature, *Proceedings of the National Academy*

of Sciences **106**, 17255 (2009).

- [79] R. Tempelaar, T. L. Jansen, and J. Knoester, Vibrational beatings conceal evidence of electronic coherence in the fmo light-harvesting complex, *The Journal of Physical Chemistry B* **118**, 12865 (2014).
 [80] J. Yuen-Zhou, J. J. Krich, I. Kassal, A. S. Johnson,

and A. Aspuru-Guzik, Ultrafast spectroscopy, IOP Publ <https://doi.org/10.1088/978-0-750-31062-8> (2014).

- [81] D. S. Bernstein and W. So, Some explicit formulas for the matrix exponential, *IEEE Transactions on Automatic Control* **38**, 1228 (1993).

Appendix A: Explicit Expressions For QFI of $|\Phi_{\text{biph,out}}\rangle$

The derivative of $|\Phi_{\text{biph,out}}\rangle$ is

$$|\partial_\theta \Phi_{\text{biph,out}}\rangle = -\frac{N_\theta}{2(1-N)^{3/2}} \sum_m r_m |\phi_m^S\rangle |\xi_m^I\rangle + \frac{1}{\sqrt{1-N}} \sum_m r_m |\partial_\theta \phi_m^S\rangle |\xi_m^I\rangle. \quad (\text{A1})$$

Then we can get the two terms of the pure state QFI as

$$\langle \partial_\theta \Phi_{\text{biph,out}} | \partial_\theta \Phi_{\text{biph,out}} \rangle = \frac{N_\theta^2}{4(1-N)^2} + \frac{1}{1-N} \sum_m |r_m|^2 \langle \partial_\theta \phi_m^S | \partial_\theta \phi_m^S \rangle - \frac{N_\theta}{(1-N)^2} \sum_m |r_m|^2 \text{Re} \langle \phi_m^S | \partial_\theta \phi_m^S \rangle, \quad (\text{A2})$$

and

$$\begin{aligned} \langle \Phi_{\text{biph,out}} | \partial_\theta \Phi_{\text{biph,out}} \rangle &= -\frac{N_\theta}{2(1-N)^2} \sum_m |r_m|^2 \langle \phi_m^S | \phi_m^S \rangle + \frac{1}{1-N} \sum_m |r_m|^2 \langle \phi_m^S | \partial_\theta \phi_m^S \rangle \\ &= -\frac{N_\theta}{2(1-N)} + \frac{1}{1-N} \sum_m |r_m|^2 \langle \phi_m^S | \partial_\theta \phi_m^S \rangle. \end{aligned} \quad (\text{A3})$$

The QFI, using Eq. (8), is

$$\begin{aligned} \mathcal{Q}(\theta; |\Phi_{\text{biph,out}}\rangle) &= \frac{N_\theta^2}{4(1-N)^2} + \frac{1}{1-N} \sum_m |r_m|^2 \langle \partial_\theta \phi_m^S | \partial_\theta \phi_m^S \rangle - \frac{N_\theta}{(1-N)^2} \sum_m |r_m|^2 \text{Re} \langle \phi_m^S | \partial_\theta \phi_m^S \rangle \\ &\quad - \frac{N_\theta^2}{4(1-N)^2} - \frac{1}{(1-N)^2} \left| \sum_m |r_m|^2 \langle \phi_m^S | \partial_\theta \phi_m^S \rangle \right|^2 + \frac{N_\theta}{(1-N)^2} \sum_m |r_m|^2 \text{Re} \langle \phi_m^S | \partial_\theta \phi_m^S \rangle \\ &= \frac{1}{1-N} \sum_m |r_m|^2 \langle \partial_\theta \phi_m^S | \partial_\theta \phi_m^S \rangle - \frac{1}{(1-N)^2} \left| \sum_m |r_m|^2 \langle \phi_m^S | \partial_\theta \phi_m^S \rangle \right|^2. \end{aligned} \quad (\text{A4})$$

Appendix B: Relative Magnitudes of QFI Contributions in Table I

1. $\Gamma_\perp \ll \Gamma$

We can calculate orders of the various terms in Eq. (37) by letting M-E coupling strength $\Gamma_\perp \rightarrow 0$ while M-S coupling strength Γ remains finite in this limit.

Expanding the matrix exponential in the characteristic response function of the molecule M, defined in Eq. (31), we have $f_M(t) \propto O(1)$, in orders of Γ as well as Γ_\perp , which in turn means $N \propto O(\Gamma\Gamma_\perp)$.

The orders of the parametric N -derivative, $N_\theta = \partial N / \partial \theta$ depend on the parameter of interest. For $\theta \equiv \Gamma$, $N_\Gamma \propto O(\Gamma_\perp)$, while for molecular Hamiltonian H_I^M parameters, it can be worked out that $N_\theta \propto O(\Gamma\Gamma_\perp)$. This then gives, for Γ parameter, $\mathcal{C}(N, 1-N) \propto O(\Gamma_\perp^2 / \Gamma\Gamma_\perp)$, meaning $\lim_{\Gamma_\perp / \Gamma \rightarrow 0} \mathcal{C}(N, 1-N) = 0$. For the molecular Hamiltonian parameters, we get similarly, $\mathcal{C}(N, 1-N) \propto O(\Gamma^2 \Gamma_\perp^2 / \Gamma\Gamma_\perp)$, which again yields $\lim_{\Gamma_\perp / \Gamma \rightarrow 0} \mathcal{C}(N, 1-N) = 0$.

Moving on to the conditional idler state, we get from the unity orders of $f_M(t)$ that $\sigma^I \propto O(1)$, which yields, for both Γ as well as molecular Hamiltonian parameters, $L_\theta \propto O(1)$, and $N\mathcal{Q}(\Gamma; \sigma^I) \propto O(\Gamma\Gamma_\perp)$, yielding a vanishing contribution in the limit of $\Gamma_\perp / \Gamma \rightarrow 0$.

2. $\Gamma_\perp \gg \Gamma$

Next, we establish the vanishingly small contribution of the biphoton QFI term $(1 - N) \mathcal{Q}(\theta; |\Phi_{\text{biph,out}}\rangle)$ in Eq. (37) in the limit of $\Gamma_\perp \gg \Gamma$. This limit can be interpreted, in turn, as $\Gamma_\perp \rightarrow 0$ for finite magnitudes of Γ , which gives $|\phi_n^S\rangle \rightarrow |\xi_n^S\rangle$, so that $|\partial_\theta \phi_n^S\rangle \rightarrow 0$. Further, utilising again the fact that $f_M(t) \propto O(1)$, we have $N \propto O(\Gamma\Gamma_\perp)$. Putting these together, we have $(1 - N) \mathcal{Q}(\theta; |\Phi_{\text{biph,out}}\rangle) \rightarrow 0$, following from Eq. (38).

Appendix C: Signal-to-Idler 1-LOCC Scheme

This class of signal-to-idler 1-LOCC protocol proceeds in the following three steps (illustrated schematically in Figure 13):

- **(Prepare):** Projectively measure the signal photon in arbitrary basis $\{W|\xi_x^S\rangle\langle\xi_x^S|W^\dagger\}$, where W is a unitary operator on signal Hilbert space, *after* the M-S interaction effected by superoperator \mathcal{W}_g in Eq. (27). This amounts to the following transformation of the entangled two-photon state, given by Kraus elements $\Pi_x^S = W|\xi_x^S\rangle\langle\xi_x^S|W^\dagger \otimes \mathbf{1}^I$,

$$\begin{aligned} \rho'_{\text{out}}[W] &= \sum_x \Pi_x^{S,\dagger} |\Phi_{\text{biph,out}}\rangle\langle\Phi_{\text{biph,out}}| \Pi_x^S \\ &= \sum_x W|\xi_x^S\rangle\langle\xi_x^S|W^\dagger \otimes |\rho_x\rangle\langle\rho_x|, |\rho_x\rangle = \frac{1}{\sqrt{1-N}} \sum_n r_n \langle\xi_x^S|W^\dagger|\phi_n^S\rangle |\xi_n^I\rangle, \end{aligned} \quad (\text{C1})$$

where $|\rho_x\rangle$ are conditional states of the idler photon, the parametric dependence on the parameter θ entering through the coefficient $\langle\xi_x^S|W^\dagger|\phi_n^S\rangle$, as well as the θ -dependent quantity N .

- The outcomes of the projective measurement $\{\Pi_x^S\}$ is classically communicated to the idler substation.
- **(Measure):** The idler photon ensemble is partitioned into sub-ensembles (labelled by the signal measurement outcome $x = x_m$) that are in the conditional states $|\rho_{x=x_m}\rangle\langle\rho_{x=x_m}|$. These are now detected in measurement bases that depends on the preparation step outcome $\{\Pi_{y|x=x_m}^I\}$. The joint signal-to-idler 1-LOCC projector is then $\Pi_{x,y} = \Pi_x^S \otimes \Pi_{y|x}^I$.

The above prepare-and-measure 1-LOCC detection scheme is now one-way going signal-to-idler because the results of the signal measurement are communicated to the idler substation. An important point of difference from the idler-to-signal LOCC scheme, detailed in Section V A, is that the preparation-step quantum operation given by Kraus operators $\{\Pi_x^S\}$ does not commute with the M-S interaction \mathcal{W}_g as they happen in the same substation of the setup. It is meaningful then only to perform the preparation-step operation $\{\Pi_x^S\}$ *after* the two-photon state has been encoded with information about the parameter θ .

Analogous to the idler-to-signal LOCC scheme, we can find the optimal signal-to-idler LOCC measurements by maximizing the associated detection CFI in two steps — first over all idler measurement strategies for the subensembles $\{|\rho_x\rangle\}$ for a given W , and subsequently over all preparation-step signal unitary operators W . Formally, we can state the maximisation analogously to idler-to-signal 1-LOCC in Eq. (41) as:

$$\max_{\Pi_{y|x}^I, \Pi_x^S} \mathcal{C}(\theta|\{\Pi_{x,y} = \Pi_x^S \otimes \Pi_{y|x}^I\}) = \max_{\Pi_x^S} \left(\max_{\Pi_{y|x}^I} \mathcal{C}(\theta|\{\Pi_{x,y} = \Pi_x^S \otimes \Pi_{y|x}^I\}) \right) \text{ s.t. } \sum_x \Pi_x^S = \mathbf{1}^I, \sum_y \Pi_{y|x}^S = \mathbf{1}^I \forall x. \quad (\text{C2})$$

For a *fixed* preparation step unitary W (which fixes Π_x^S), the maximal CFI of all measurement-step detection measurements on the idler photon is equal to the QFI of the intermediate state $\rho'_{\text{out}}[W]$ as maximisation over $\{\Pi_{y|x}^I\}$ is precisely the maximisation that yields the quantum Cramér-Rao bound [33, 34] for the conditional state $\rho'_{\text{out}}[W]$ (in analogy with the idler-to-signal measurement-optimal 1-LOCC):

$$\mathcal{C}_{\text{max}}(\theta; W) = \mathcal{Q}(\theta; \rho'_{\text{out}}[W]) = \mathcal{Q}(\theta; \sum_x W|\xi_x^S\rangle\langle\xi_x^S|W^\dagger \otimes |\rho_x\rangle\langle\rho_x|). \quad (\text{C3})$$

where $\mathcal{C}_{\text{max}}(\theta; W)$ is the CFI of measurement-optimal LOCC strategy for a given W , defined as the LOCC protocol that has maximal CFI for fixed W . By renormalizing the conditional states $|\rho'_x\rangle = \frac{1}{\sqrt{\langle\rho_x|\rho_x\rangle}}|\rho_x\rangle$ in order to express

$\rho'_{\text{out}}[W]$ in its spectral form, we can use Eq. (9) to evaluate the measurement-step-maximal CFI explicitly,

$$\begin{aligned} \mathcal{C}_{\text{max}}(\theta; W) &= \sum_x \frac{(\partial_\theta \langle \rho_x | \rho_x \rangle)^2}{\langle \rho_x | \rho_x \rangle} + \frac{4}{1-N} \sum_m |r_m|^2 \langle \partial_\theta \phi_m^S | \partial_\theta \phi_m^S \rangle - \sum_x \langle \rho_x | \rho_x \rangle |\langle \rho'_x | \partial_\theta \rho'_x \rangle|^2 \\ &= \frac{4}{1-N} \sum_m |r_m|^2 \langle \partial_\theta \phi_m^S | \partial_\theta \phi_m^S \rangle - \frac{4}{(1-N)^2} \sum_x \frac{1}{\langle \rho_x | \rho_x \rangle} (\text{Im} \langle \rho_x | \partial_\theta \rho_x \rangle^2 - \text{Re} \langle \rho_x | \partial_\theta \rho_x \rangle^2) \end{aligned} \quad (\text{C4})$$

where

$$\langle \rho_x | \rho_x \rangle = \frac{1}{1-N} \sum_m |r_m|^2 |\langle \xi_x^S | W^\dagger | \phi_m^S \rangle|^2 \quad (\text{C5})$$

has parametric dependence on θ , just as for the idler-to-signal scheme. The overlap can be expressed in the more succinct form

$$\langle \rho_x | \partial_\theta \rho_x \rangle = \frac{1}{1-N} \langle \xi_x^S | W^\dagger Y W | \xi_x^S \rangle \quad (\text{C6})$$

where

$$Y(\theta) = \sum_{m,n} |r_n|^2 \langle \phi_m^S | \partial_\theta \phi_n^S \rangle | \phi_m^S \rangle \langle \phi_n^S | \quad (\text{C7})$$

is an operator on the signal Hilbert space. The measurement-optimal CFI for signal-to-idler LOCC scheme for given W then has the following form:

$$\begin{aligned} \mathcal{C}_{\text{max}}(\theta; W) &= \frac{4}{1-N} \sum_m |r_m|^2 \langle \partial_\theta \phi_m^S | \partial_\theta \phi_m^S \rangle \\ &\quad - \frac{4}{(1-N)^2} \sum_x \frac{1}{\sum_m |r_m|^2 |\langle \xi_x^S | W^\dagger | \phi_m^S \rangle|^2} (\text{Im}(\langle \xi_x^S | W^\dagger Y W | \xi_x^S \rangle)^2 - \text{Re}(\langle \xi_x^S | W^\dagger Y W | \xi_x^S \rangle)^2) \end{aligned} \quad (\text{C8})$$

Note both the similarity of expressions to the idler-to-signal LOCC case in Eq. (D3), as well as the differences – the expressions for measurement-step-maximal CFI are not the same because the biphoton setup is not symmetrical, as we have remarked before.

We can now similarly obtain the overall optimal signal-to-idler LOCC measurement that fetches the maximal value of measurement CFI for *any* W . This is done by maximizing the functional $\mathcal{C}_{\text{max}}(\theta; W)$ over the set of all unitary matrices W , which amounts to a minimisation of the second term in Eq. (C4). Defining the cost function as

$$\varpi(\theta; W) = \frac{4}{(1-N)^2} \sum_x \frac{1}{\sum_m |r_m|^2 |\langle \xi_x^S | W^\dagger | \phi_m^S \rangle|^2} (\text{Im}(\langle \xi_x^S | W^\dagger Y W | \xi_x^S \rangle)^2 - \text{Re}(\langle \xi_x^S | W^\dagger Y W | \xi_x^S \rangle)^2), \quad (\text{C9})$$

where $\varpi(\theta; W) \geq 0$ (which follows from $\mathcal{Q}(\theta; \rho'_{\text{out}}[W]) \geq 0$), and the optimal unitary transformation W_{opt} is defined as:

$$W_{\text{opt}} : \varpi(\theta; W_{\text{opt}}) \leq \varpi(\theta; W) \quad \forall W \text{ s.t. } W^\dagger W = \mathbb{1}^S. \quad (\text{C10})$$

The overall maximal CFI for idler-to-signal prepare-and-measure LOCC is then

$$\mathcal{C}_{S \rightarrow I}(\theta) = \frac{4}{1-N} \sum_m |r_m|^2 \langle \partial_\theta \phi_m^S | \partial_\theta \phi_m^S \rangle - \varpi(\theta; W_{\text{opt}}). \quad (\text{C11})$$

a. Lower Bound

Just like the idler-to-signal scenario, the measurement-optimal CFI $\mathcal{C}_{\text{max}}(\theta; W)$ can be lower bounded using the convexity of the quantum Fisher information:

$$\begin{aligned} \mathcal{C}_{\text{max}}(\theta; W) &= \mathcal{Q}(\theta; \rho'_{\text{out}}[W]) = \mathcal{Q}\left(\theta; \sum_x W | \xi_x^S \rangle \langle \xi_x^S | W^\dagger \otimes | \rho_x \rangle \langle \rho_x | \right) \\ &\geq \mathcal{Q}(\theta; \text{Tr}_I \rho'_{\text{out}}[W]) = \mathcal{Q}\left(\theta; \sum_x \langle \xi_x^S | W^\dagger \text{Tr}_I | \Phi_{\text{biph,out}} \rangle \langle \Phi_{\text{biph,out}} | W | \xi_x^S \rangle W | \xi_x^S \rangle \langle \xi_x^S | W^\dagger \right) \\ &= \mathcal{C}(\theta; \langle \xi_x^S | W^\dagger \text{Tr}_I | \Phi_{\text{biph,out}} \rangle \langle \Phi_{\text{biph,out}} | W | \xi_x^S \rangle) \geq \mathcal{Q}(\theta; \text{Tr}_I | \Phi_{\text{biph,out}} \rangle) \end{aligned} \quad (\text{C12})$$

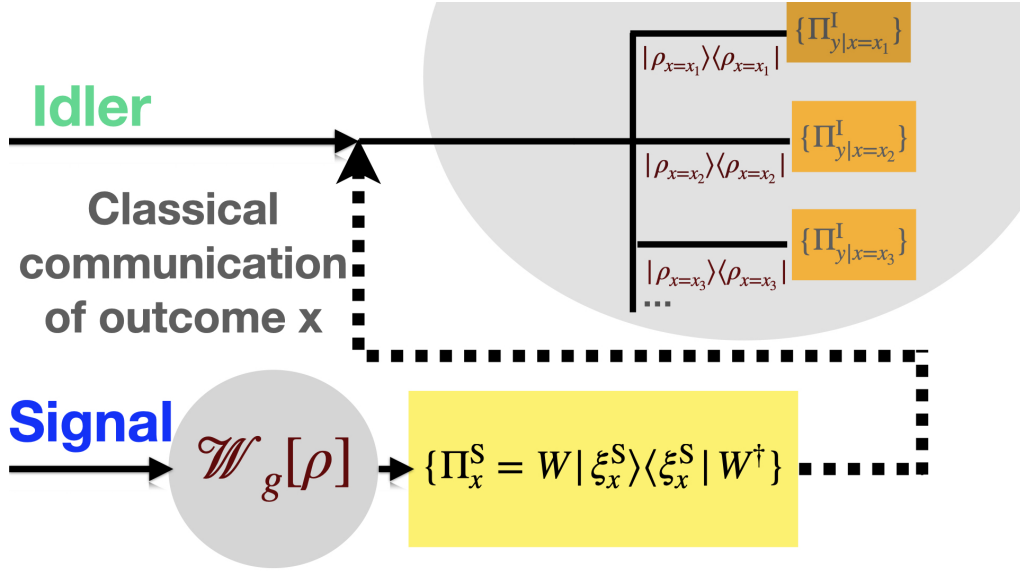


Figure 13. Signal-to-idler prepare-and-measure LOCC scheme. The two-photon Kraus operators for the overall LOCC scheme are given as $\{\Pi_{x,y} = \Pi_x^S \otimes \Pi_y^I\}$

which is identical to the lower bound in Eq. (51) for the idler-to-signal protocol QFI. The second inequality in the above chain may always be saturated for single-parameter estimation with an appropriate choice for W . By the same reasoning as the idler-to-signal case, the first inequality is saturated iff $\langle\phi_m^S|\partial_\theta\phi_n^S\rangle = 0 \forall m, n$ (see Eq. (9)). For a Schmidt basis $\{|\phi_n^S\rangle\}$ that is complete on the signal Hilbert space, this is never satisfied, and we get the stronger inequality

$$\mathcal{C}_{\max}(\theta; W) > \mathcal{Q}(\theta; \text{Tr}_I|\Phi_{\text{biph,out}}\rangle). \quad (\text{C13})$$

This then leads to the following hierarchy of Fisher informations:

$$\mathcal{Q}(\theta; |\Phi_{\text{biph,out}}\rangle) \geq \mathcal{C}_{S \rightarrow I}(\theta) \geq \mathcal{C}_{\max}(\theta; W) > \mathcal{Q}(\theta; \text{Tr}_I|\Phi_{\text{biph,out}}\rangle). \quad (\text{C14})$$

Therefore, the reduced signal state QFI $\mathcal{Q}(\theta; \text{Tr}_I|\Phi_{\text{biph,out}}\rangle)$ serves as a useful benchmark for the effectiveness of LOCC parameter estimation using entangled light. For the signal-to-idler scheme, practical difficulties for a setup requiring the preparation step to necessarily follow the light-matter interaction make this LOCC scheme much less attractive as a means for enhanced θ -estimation compared to idler-to-signal scheme, where the idler photon is conditioned by preparation POVMs independent of interaction with the sample and subsequent measurement in the signal mode.

Appendix D: Optimal 1-LOCC Measurement Projectors for Biphoton Setup

As indicated by the RHS of Eq. (41), the maximisation of the 1-LOCC CFI function can proceed in two steps: first, for a fixed unitary transformation V , we maximise over all signal POVMs $\{\Pi_{y|x=x_m}^S\}$; in the second step, the resulting quantity is then maximised over all choices of unitary preparation V .

1. Optimisation over signal POVM $\{\Pi_{y|x=x_m}^S\}$

For a *fixed* V , maximisation of the CFI over $\{\Pi_{y|x=x_m}^S\}$ is precisely the maximisation that yields the Cramér-Rao bound [33, 34] for the conditional state $\rho'_{\text{out}}[V]$, meaning that

$$\mathcal{C}_{\max}(\theta; V) = \mathcal{Q}(\theta; \rho'_{\text{out}}[V]). \quad (\text{D1})$$

Abbreviating normalised conditional states

$$|\zeta'_x\rangle = \frac{1}{\sqrt{\langle\zeta_x|\zeta_x\rangle}}|\zeta_x\rangle, \quad (\text{D2})$$

and using Eq. (9),

$$\mathcal{C}_{\max}(\theta; V) = \sum_x \langle \zeta_x | \zeta_x \rangle \mathcal{Q}(\theta; |\zeta'_x\rangle \langle \zeta'_x|) + \mathcal{C}(\theta; \{ \langle \zeta_x | \zeta_x \rangle \}), \quad (\text{D3})$$

where

$$\sum_x \langle \zeta_x | \zeta_x \rangle \mathcal{Q}(\theta; |\zeta'_x\rangle \langle \zeta'_x|) = \frac{4}{1-N} \sum_m |r_m|^2 \langle \partial_\theta \phi_m^S | \partial_\theta \phi_m^S \rangle - \frac{1}{(1-N)^2} \sum_x \frac{4}{\langle \zeta_x | \zeta_x \rangle} |\langle \xi_x^I | V^\dagger X(\theta) V | \xi_x^I \rangle|^2, \quad (\text{D4})$$

and

$$X(\theta) = \sum_{m,n} r_m r_n^* \langle \phi_n^S | \partial_\theta \phi_m^S \rangle |\xi_m^I\rangle \langle \xi_n^I| \quad (\text{D5})$$

is an operator on the idler I space. The one other orthonormal basis vector (besides $|\Phi_{\text{biph,out}}\rangle$) in the two-dimensional $\text{Span}[|\Phi_{\text{biph,out}}\rangle, |\partial_\theta \Phi_{\text{biph,out}}\rangle]$ can be constructed as [35]

$$|\Phi_{\text{biph,out}}^\perp\rangle \equiv (1 - |\Phi_{\text{biph,out}}\rangle \langle \Phi_{\text{biph,out}}|) |\partial_\theta \Phi_{\text{biph,out}}\rangle, \quad (\text{D6})$$

in terms of which

$$X = (1-N) \text{Tr}_S |\Phi_{\text{biph,out}}\rangle \langle \Phi_{\text{biph,out}}^\perp| + \text{Tr}(X) \text{Tr}_S |\Phi_{\text{biph,out}}\rangle \langle \Phi_{\text{biph,out}}|, \quad (\text{D7})$$

where

$$\text{Tr}(X) = \left[(1-N) \langle \Phi_{\text{biph,out}} | \partial_\theta \Phi_{\text{biph,out}} \rangle - \frac{N_\theta}{2} \right]. \quad (\text{D8})$$

The relation in Eq. (D7) can be obtained using Eq. (D6), and noting that

$$\text{Tr}_S |\partial_\theta \Phi_{\text{biph,out}}\rangle \langle \Phi_{\text{biph,out}}| = \frac{N_\theta}{2(1-N)} \text{Tr}_S |\Phi_{\text{biph,out}}\rangle \langle \Phi_{\text{biph,out}}| + \frac{X}{1-N}. \quad (\text{D9})$$

Finally, we can also recast Eq. (38) in terms of X :

$$\mathcal{Q}(\theta; |\Phi_{\text{biph,out}}\rangle) = \frac{4}{1-N} \sum_n |r_n|^2 \langle \phi_n^S | \phi_n^S \rangle - \frac{4}{(1-N)^2} |\text{Tr}(X)|^2, \quad (\text{D10})$$

where we have employed the explicit relation $\text{Tr}(X) = \sum_n |r_n|^2 \langle \phi_n^S | \partial_\theta \phi_n^S \rangle$.

2. Optimal Choice of Preparation Unitary V

Eq. (D3) is the Fisher information corresponding to the optimal 1-LOCC θ -estimation strategy for a given unitary V , obtained by maximising the CFI functional over the set of measurement POVMs $\{\Pi_{y|x}^S\}$ acting on the sub-ensemble states of the signal photon $\{|\zeta'_x\rangle\}$. To identify the optimal 1-LOCC detection scheme that fetches the maximum CFI, we now proceed to maximise $\mathcal{C}_{\max}(\theta; V)$ over all V . As only the second term on the RHS of Eq. (D4) depends on V , we can see that the maximisation is equivalent to minimisation of the following cost function:

$$\vartheta(\theta; V) = \frac{1}{(1-N)^2} \sum_x \frac{4}{\langle \zeta_x | \zeta_x \rangle} |\langle \xi_x^I | V^\dagger X(\theta) V | \xi_x^I \rangle|^2 - \mathcal{C}(\theta; \{ \langle \zeta_x | \zeta_x \rangle \}). \quad (\text{D11})$$

Using the inequality chain

$$\mathcal{C}_{\max}(\theta; V) \leq \mathcal{C}_{\max}(\theta; V_0) < \mathcal{Q}(\theta, |\Phi_{\text{biph,out}}\rangle), \quad (\text{D12})$$

we have for the cost function

$$\vartheta(\theta; V) \geq \vartheta(\theta; V_{\text{opt}}) > \frac{4}{(1-N)^2} |\text{Tr}(X)|^2, \quad (\text{D13})$$

where V_{opt} is the optimal unitary, defined formally as

$$V_{\text{opt}} : \vartheta(\theta; V_{\text{opt}}) \leq \vartheta(\theta; V) \quad \forall V \text{ s.t. } V^\dagger V = \mathbf{1}^I, \quad (\text{D14})$$

and the second inequality in Eq. (D13) follows from Eq. (D10).

Our strategy in the following will be to construct a preparation unitary that saturates the latter of the inequalities in Eq. (D13). While the existence of such a unitary (and hence a 1-LOCC detection) is not guaranteed for general multipartite scenarios, showing that there exists such a unitary preparation for which the inequality is saturated is a *sufficient* condition for maximisation. This follows from the fact that measurement CFIs can never exceed the QFI.

3. Proof of Theorem 1

For the traceless (in I space) compact bounded operator $\text{Tr}_S |\Phi_{\text{biph,out}}\rangle\langle\Phi_{\text{biph,out}}^\perp|$, we can always construct [62, 69] a preparation-step unitary V_0 such that

$$\langle\xi_m^I|V_0^\dagger \text{Tr}_S |\Phi_{\text{biph,out}}\rangle\langle\Phi_{\text{biph,out}}^\perp|V_0|\xi_m^I\rangle = 0 \quad \forall m, \quad (\text{D15})$$

A short calculation then reveals that (which we will establish separately below)

$$\vartheta(\theta; V_0) = \frac{1}{(1-N)^2} |\text{Tr}(X)|^2, \quad (\text{D16})$$

from which $\mathcal{C}_{\text{max}}(\theta, V_0) = \mathcal{Q}(\theta; |\Phi_{\text{biph,out}}\rangle)$ follows, establishing Theorem 1. Thus for all unitary preparations V_0 that admit the condition in Eq. (D16), the corresponding measurement-optimal 1-LOCC saturates the ultimate quantum Crámer-Rao bound.

a. $V = V_0$ saturates cost function $\vartheta(\theta; V)$ bound

In order to establish the relation in Eq. (D16), we first note that

$$\begin{aligned} \langle\xi_x|V_0^\dagger X V_0|\xi_x\rangle &= \langle\xi_x|V_0^\dagger (1-N)\text{Tr}_S |\Phi_{\text{biph,out}}^\perp\rangle\langle\Phi_{\text{biph,out}}|V_0|\xi_x\rangle + \text{Tr}(X) \langle\xi_x|V_0^\dagger \text{Tr}_S |\Phi_{\text{biph,out}}\rangle\langle\Phi_{\text{biph,out}}|V_0|\xi_x\rangle \\ &= \text{Tr}(X) \langle\zeta_x|\zeta_x\rangle. \end{aligned} \quad (\text{D17})$$

where we have used the optimality relation for V_0 in Eq. (D15) in the first line, and the second line utilises the relation

$$\langle\xi_x|V_0^\dagger \text{Tr}_S |\Phi_{\text{biph,out}}\rangle\langle\Phi_{\text{biph,out}}|V_0|\xi_x\rangle = \langle\zeta_x|\zeta_x\rangle \quad (\text{D18})$$

which can be easily worked out explicitly. The cost function in Eq. (D11) then becomes

$$\begin{aligned} \vartheta(\theta; V_0) &= \frac{1}{(1-N)^2} \sum_x \frac{1}{\langle\zeta_x|\zeta_x\rangle} \langle\zeta_x|\zeta_x\rangle^2 |\text{Tr}(X)|^2 + \mathcal{C}(\theta; \langle\zeta_x|\zeta_x\rangle) \\ &= \frac{1}{(1-N)^2} |\text{Tr}(X)|^2 \sum_x \frac{1}{1-N} r_m^* r_n (V_0)_{mx} (V_0)_{nx}^* \langle\phi_m|\phi_n\rangle + \mathcal{C}(\theta; \langle\zeta_x|\zeta_x\rangle) = \frac{|\text{Tr}(X)|^2}{(1-N)^2} + \mathcal{C}(\theta; \langle\zeta_x|\zeta_x\rangle) \end{aligned} \quad (\text{D19})$$

where we have used the unitarity of the V_0 matrix : $\sum_x (V_0)_{mx} (V_0)_{nx}^* = \delta_{mn}$. The second step will be to establish that the classical Fisher information $\mathcal{C}(\theta; \langle\zeta_x|\zeta_x\rangle)$ corresponding to mixing of the subensemble states $\{|\zeta'_x\rangle\}$ vanishes for unitary V_0 . In order to do this, we first look at the structure of the inner product

$$\begin{aligned} \langle\zeta_x|\partial_\theta\zeta_x\rangle &= \frac{N_\theta}{2(1-N)} \langle\zeta_x|\zeta_x\rangle + \frac{1}{1-N} \langle\xi_x|V_0^\dagger X V_0|\xi_x\rangle = \left(\frac{N_\theta}{2(1-N)} + \text{Tr}(X) \right) \langle\zeta_x|\zeta_x\rangle \\ &= \langle\Phi_{\text{biph,out}}|\partial_\theta\Phi_{\text{biph,out}}\rangle \langle\zeta_x|\zeta_x\rangle \end{aligned} \quad (\text{D20})$$

where we have used the relation $\langle\xi_x|V_0^\dagger X V_0|\xi_x\rangle = \text{Tr}(X) \langle\zeta_x|\zeta_x\rangle$ in the first line, and Eq. (D8) in the second line. Now, keeping in mind that the outgoing biphoton state $|\Phi_{\text{biph,out}}\rangle$ is a normalised quantum state, we have $\langle\Phi_{\text{biph,out}}|\Phi_{\text{biph,out}}\rangle = 1$, and thence $\text{Re} \langle\Phi_{\text{biph,out}}|\partial_\theta\Phi_{\text{biph,out}}\rangle = 0$. This then gives

$$\mathcal{C}(\theta; \{\langle\zeta_x|\zeta_x\rangle\}) = \sum_x 4 \frac{\langle\zeta_x|\partial_\theta\zeta_x\rangle^2}{\langle\zeta_x|\zeta_x\rangle} = \sum_x 4 \langle\zeta_x|\zeta_x\rangle \text{Re} \langle\Phi_{\text{biph,out}}|\partial_\theta\Phi_{\text{biph,out}}\rangle^2 = 0, \quad (\text{D21})$$

which proves Eq. (D16).

Briefly, we also note that a similar result was established recently for multipartite pure and rank 2 states in finite-dimensional Hilbert spaces [62]. However, the recipe can not be generalised to our infinite-dimensional CV case due to its dependence on the total system dimension. We have thus employed a different and more direct approach here that establishes existence of 1-LOCC schemes whose CFI is shown to equal the QFI for the outgoing state.

Appendix E: Parametric Relation Between PDC Entanglement and Outgoing QFI

This appendix contains parametric plots depicting the relationship between entanglement of input time-frequency entangled states, as captured by entropy of entanglement defined in Eq. (57), and outgoing biphoton QFI $Q(\theta; |\Phi_{\text{PDC},\text{out}}\rangle)$. Figure 14 (a)-(b) shows these plots for TLS parameters, while (c)-(d) display the same relationship for CD parameter J , all for PDC input states in Eq. (56). Figure 15 shows analogous plots for TFM states defined in Eq. (69).

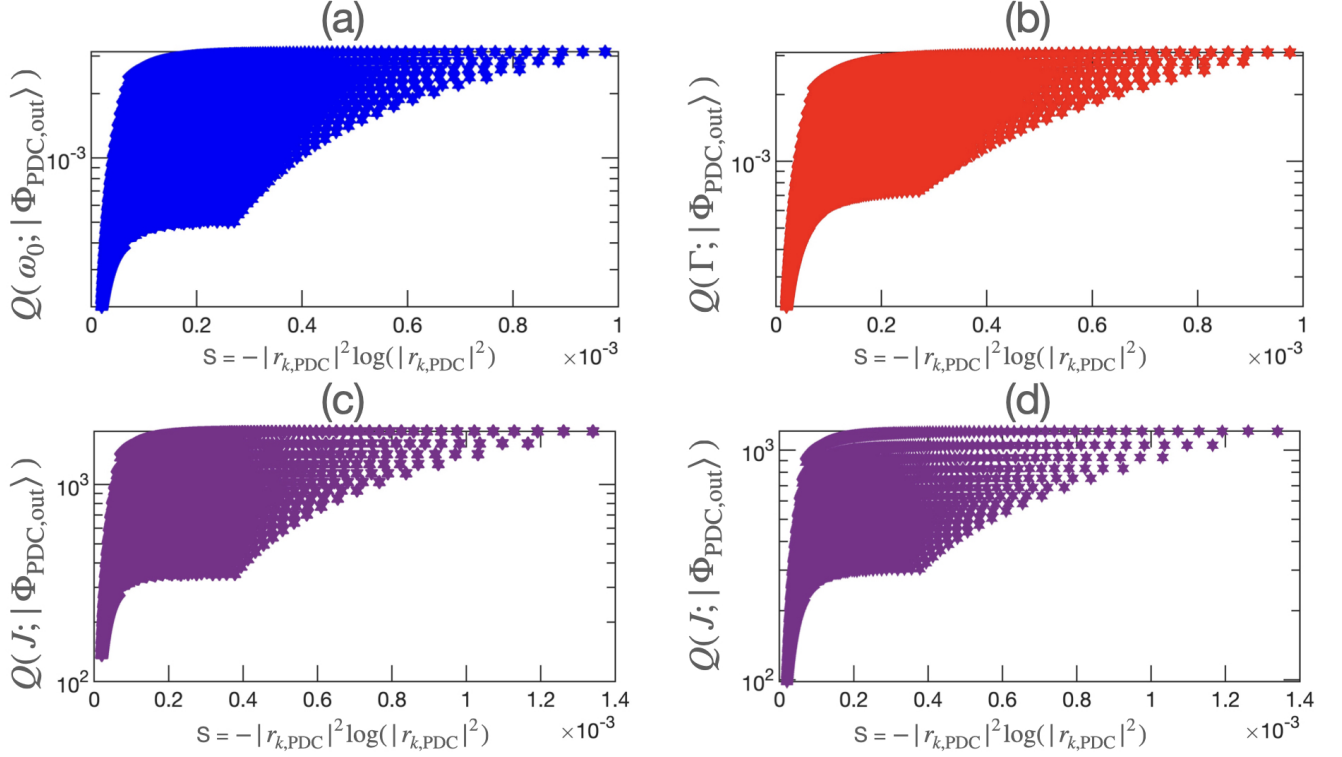


Figure 14. Scatter plots of outgoing entangled beam QFI $Q(\theta; |\Phi_{\text{PDC},\text{out}}\rangle)$, plotted as a function of entanglement entropy $S = -|r_{k,\text{PDC}}|^2 \log(|r_{k,\text{PDC}}|^2)$ in the incoming state $|\Phi_{\text{PDC}}\rangle$, for (a) TLS parameter $\theta \equiv \omega_0$ (corresponding to Figure 5(a)), (b) TLS parameter $\theta \equiv \Gamma$ (corresponding to Figure 5(b)), (c) CD parameter J for $\bar{\omega}_S = \omega_\alpha$ (corresponding to Figure 10(a)), and (d) CD parameter J for $\bar{\omega}_S = \omega_\beta$ (corresponding to Figure 10(b)). ($\Gamma = 0.15$ THz $\Gamma_\perp = 0$)

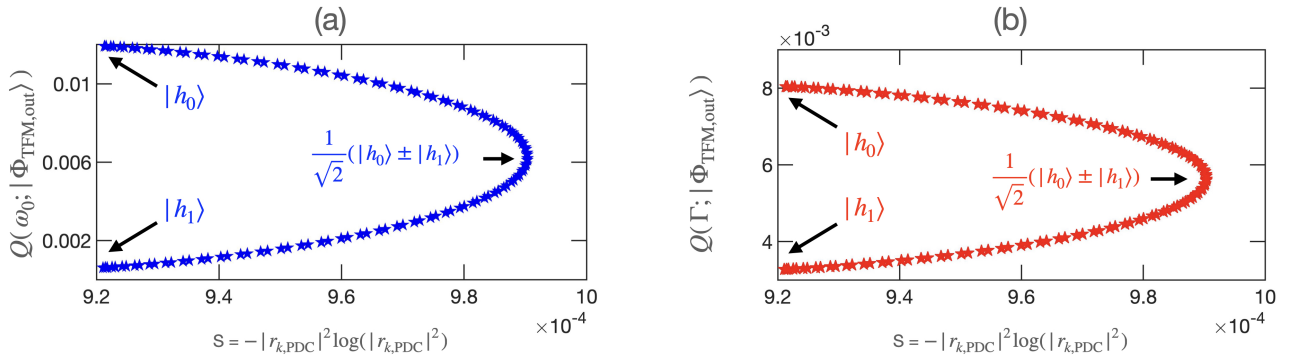


Figure 15. Parametric plot of outgoing TFM state QFI $Q(\theta; |\Phi_{\text{TFM},\text{out}}\rangle)$, plotted as a function of entanglement entropy $S = -|r_{k,\text{PDC}}|^2 \log(|r_{k,\text{PDC}}|^2)$ in the incoming state $|\Phi_{\text{TFM}}\rangle$ (defined in Eq. (69)), for (a) TLS parameter $\theta \equiv \omega_0$, and (b) TLS parameter $\theta \equiv \Gamma$. ($k_1 = k_2 = 1.3$ ps, $\Gamma = 0.15$ THz, $\Gamma_\perp = 0$ THz, $\Delta = 0$.)

Appendix F: TLS Estimation Using PDC Light with $\Delta > 0$

The following series of plots reproduce all quantities presented in Section VI B for TLS parameter estimation using PDC light, but now for nonzero detuning between the central paraxial frequency $\bar{\omega}_S$, and TLS frequency ω_0 .

1. Perfect Coupling

Outgoing PDC state QFI for TLS parameter Γ for $\Delta \neq 0$

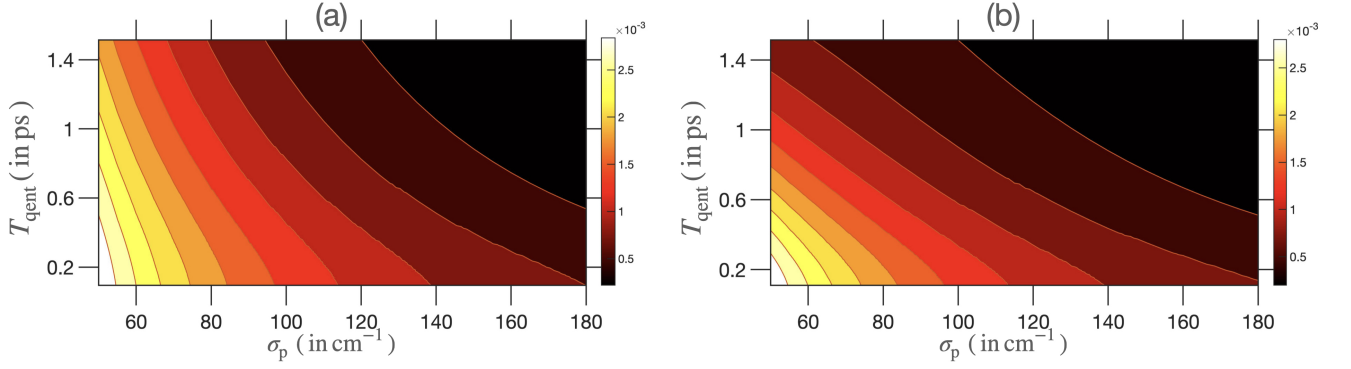


Figure 16. Outgoing entangled beam QFI $\mathcal{Q}(\Gamma; |\Phi_{\text{PDC, out}}\rangle)$, calculated numerically using Eq. (62), for varying entanglement time T_{qent} , and classical pumpwidth σ_p , for TLS parameter Γ and detunings (a) $\Delta = 20$ THz, and (b) $\Delta = 100$ THz. ($\Gamma = 0.15$ THz, $\Gamma_{\perp} = 0$ THz.)

Outgoing PDC state QFI for TLS parameter ω_0 for $\Delta \neq 0$

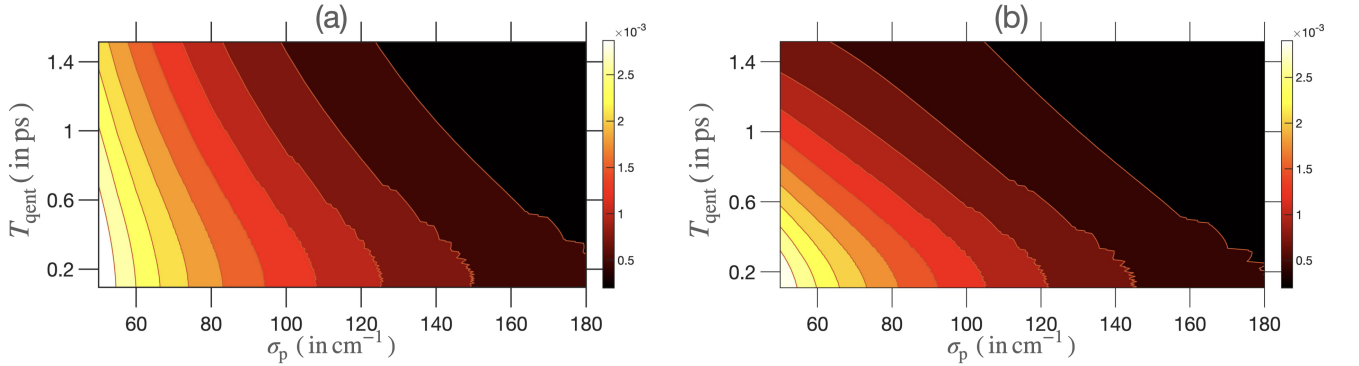


Figure 17. Outgoing entangled beam QFI $\mathcal{Q}(\omega_0; |\Phi_{\text{PDC, out}}\rangle)$, calculated numerically using Eq. (62), for varying entanglement time T_{qent} , and classical pumpwidth σ_p , for TLS parameter ω_0 and detunings (a) $\Delta = 20$ THz, and (b) $\Delta = 100$ THz. ($\Gamma = 0.15$ THz, $\Gamma_{\perp} = 0$ THz.)

In Figures 16 and 17, we see that the QFI admits the same trend with respect to σ_p and T_{qent} as Figure 5 for either TLS parameters Γ or ω_0 as the magnitude of detuning $|\Delta|$ changes, with the only noticeable effect of the detuning manifesting in the diminished magnitudes for the QFIs.

Next, in Figures 18 and 19 we plot the degree of optimality of measurement-optimal $V = \mathbb{1}^I$ LOCC, $\varkappa(\theta)$, for TLS parameters Γ and ω_0 respectively. Figure 18 displays the departure from the forecasted value of unity for $\varkappa(\Gamma)$ when there is zero detuning between ω_0 and $\bar{\omega}_S$, which can be attributed to the increasing value of the quantity $|\langle \Phi_{\text{PDC, out}} | \partial_{\Gamma} \Phi_{\text{PDC, out}} \rangle|$ as $|\Delta|$ increases. In contrast, Figure 19 shows that for certain incoming PDC states (see upper left corner of the $(\sigma_p, T_{\text{qent}})$ grid) a higher magnitude of detuning can actually enhance the optimality of the measurement-optimal $V = \mathbb{1}^I$ LOCC detection scheme. This shows that, even though the overall QFI values decrease with increasing $|\Delta|$ for either parameter (rendering therefore all possible estimators less precise), the effect of increasing

Degree of optimality $\varkappa(\Gamma)$ for TLS parameter Γ for $\Delta \neq 0$

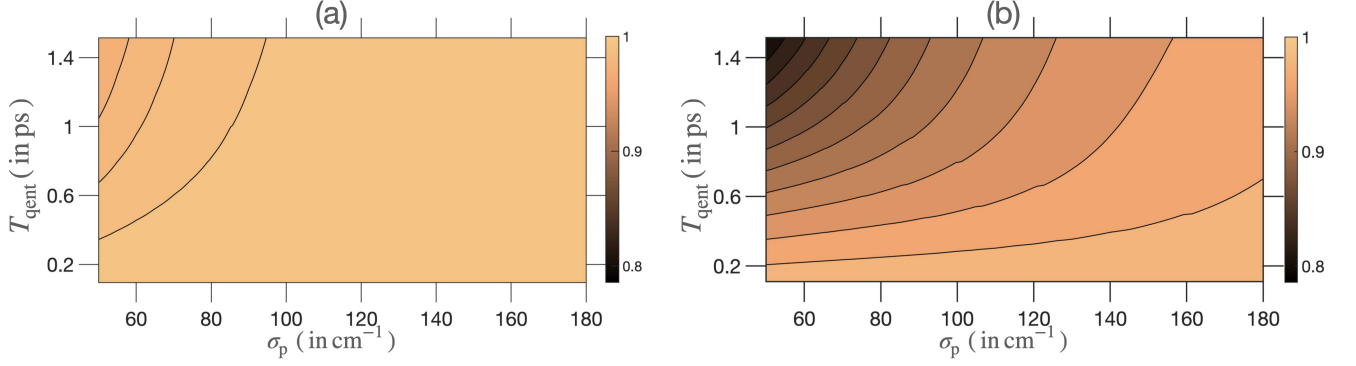


Figure 18. Degree of optimality of measurement-optimal $V = \mathbf{1}^I$ LOCC schemes, measured as the ratio $\varkappa(\Gamma)$ (defined in Eq. (71)), for estimation of TLS parameter Γ , using PDC light for detunings (a) $\Delta = 20$ THz, and (b) $\Delta = 100$ THz. ($\Gamma = 0.15$ THz)

Degree of optimality $\varkappa(\omega_0)$ for TLS parameter ω_0 for $\Delta \neq 0$

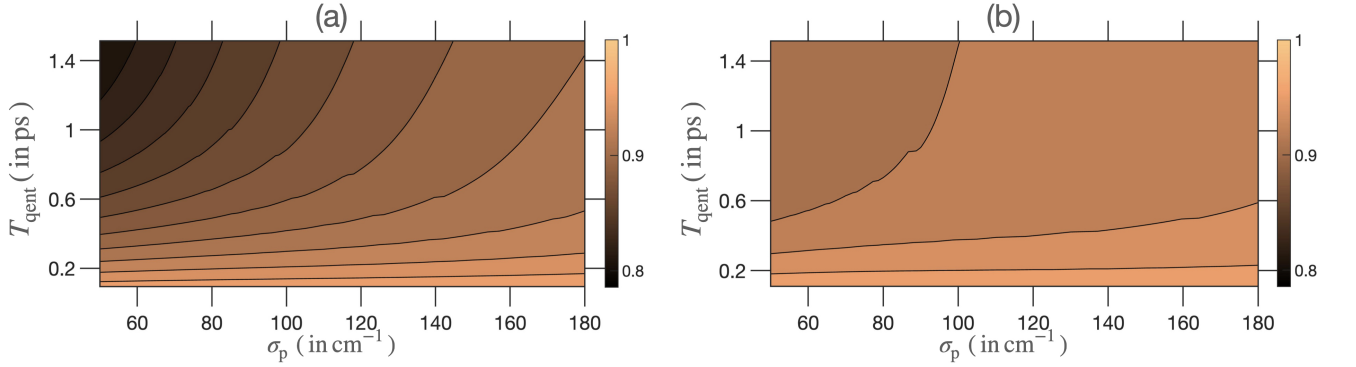


Figure 19. Degree of optimality of measurement-optimal $V = \mathbf{1}^I$ LOCC schemes, measured as the ratio $\varkappa(\omega_0)$ (defined in Eq. (71)), for estimation of TLS parameter ω_0 , using PDC light for detunings (a) $\Delta = 20$ THz, and (b) $\Delta = 100$ THz. ($\Gamma = 0.15$ THz)

detuning on the degree of optimality of measurement schemes is less certain, and may depend on the parameter of interest.

Enhancement factor $\varsigma(\Gamma)$ for TLS parameter Γ for $\Delta \neq 0$

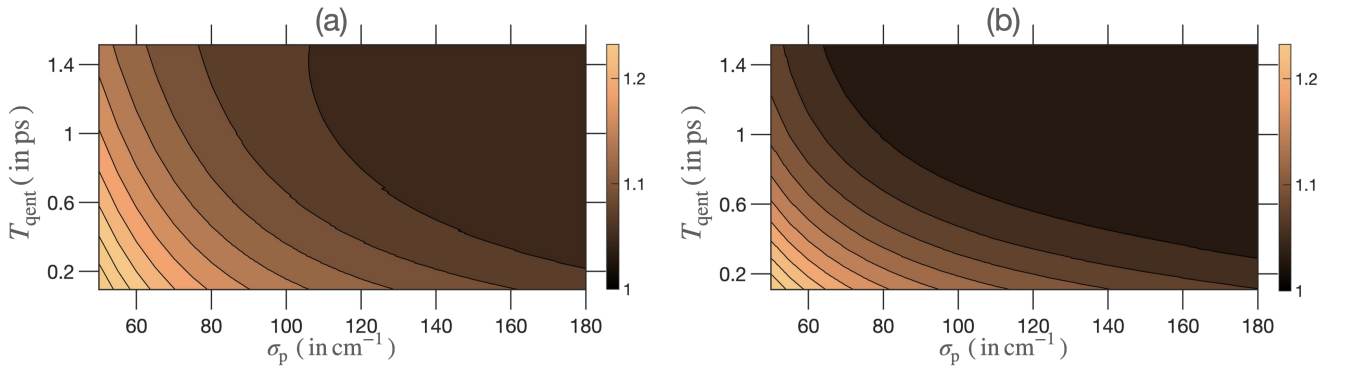


Figure 20. Enhancement factor of measurement-optimal $V = \mathbf{1}^I$ LOCC schemes, measured as the ratio $\varsigma(\Gamma)$ (defined in Eq. (72)), for estimation of TLS parameter Γ , using PDC light for detunings (a) $\Delta = 20$ THz, and (b) $\Delta = 100$ THz. ($\Gamma = 0.15$ THz)

A similar behaviour is observed in Figures 20 and 21 — for Γ -estimation using PDC photons, the enhancement $\varsigma(\Gamma)$ of $V = \mathbf{1}^I$ over all single-mode schemes decreases as detuning increases (Figure 20), whereas for ω_0 -estimation, a

Enhancement factor $\zeta(\omega_0)$ for TLS parameter ω_0 for $\Delta \neq 0$

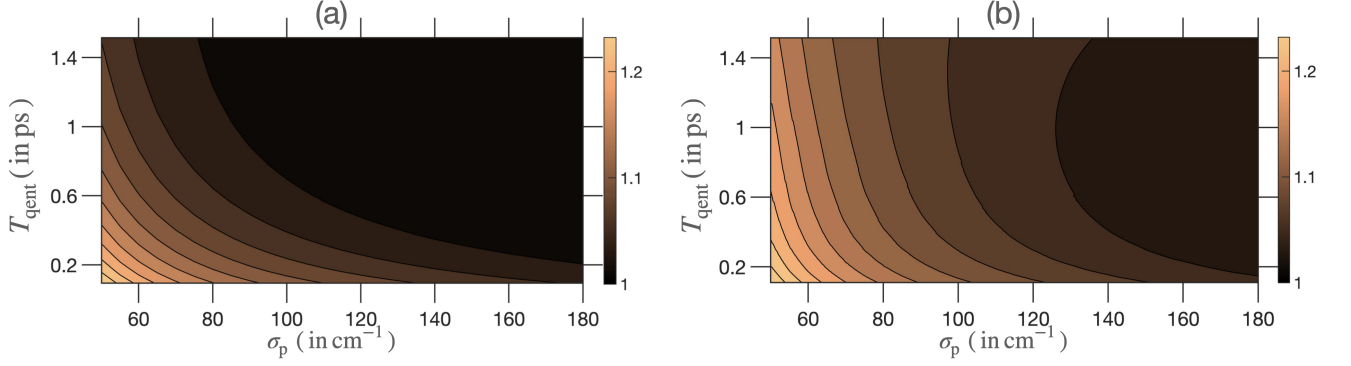


Figure 21. Enhancement factor of measurement-optimal $V = \mathbb{1}^I$ LOCC schemes, measured as the ratio $\zeta(\omega_0)$ (defined in Eq. (72)), for estimation of TLS parameter ω_0 , using PDC light for detunings (a) $\Delta = 20$ THz, and (b) $\Delta = 100$ THz. ($\Gamma = 0.15$ THz)

Outgoing PDC state QFI for TLS parameter Γ for $\Delta \neq 0$ ($\Gamma_{\perp}/\Gamma = 0.5$)

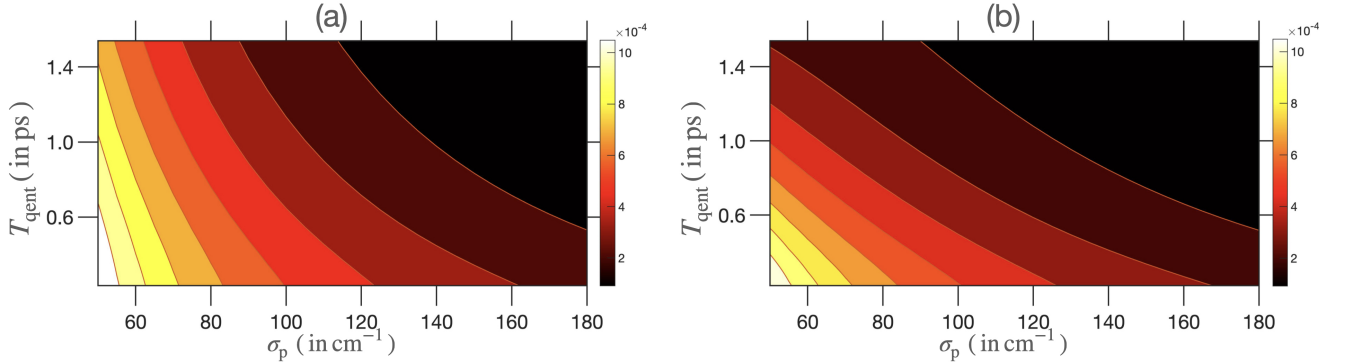


Figure 22. Outgoing entangled beam QFI $\mathcal{Q}(\Gamma; |\Phi_{\text{PDC, out}}\rangle)$, calculated numerically using Eq. (37), for varying entanglement time T_{qent} , and classical pumpwidth σ_p , for TLS parameter Γ and detunings (a) $\Delta = 20$ THz, and (b) $\Delta = 100$ THz. ($\Gamma = 0.15$ THz, $\Gamma_{\perp}/\Gamma = 0.5$.)

larger enhancement $\zeta(\omega_0)$ can be obtained using PDC states with signal photon far detuned from the TLS frequency ω_0 (Figure 21).

2. Free Space $\Gamma_{\perp} > 0$

We can also study the effect of non-zero detuning on TLS estimation for the free space scenario, characterised by non-zero coupling to E space $\Gamma_{\perp} > 0$. In Figures 22 and 23, we plot Γ -QFI for the same grid of PDC characteristics σ_p and T_{qent} as Figure 8. Again, the trend for QFI values against PDC characteristics σ_p and T_{qent} remains unchanged, with moderately diminishing values for the QFI as detuning increases. A similar effect is seen for the TLS parameter ω_0 in Figures 24 and 25 for free space couplings $\Gamma_{\perp}/\Gamma = 0.5$ and $\Gamma_{\perp}/\Gamma = 10.0$ respectively.

Appendix G: Light-CD Interaction In Excitonic Basis

The coupled dimer (CD) system is comprised of two two-level systems, coupled to each other via an attractive Coulomb interaction, so that the bare molecular Hamiltonian is

$$H^{\text{CD}} = \sum_{j=a,b} \hbar\omega_j |j\rangle\langle j| + \hbar(\omega_a + \omega_b) |f\rangle\langle f| + J(|a\rangle\langle b| + |b\rangle\langle a|), \quad (\text{G1})$$

Outgoing PDC state QFI for TLS parameter Γ for $\Delta \neq 0$ ($\Gamma_{\perp}/\Gamma = 10.0$)

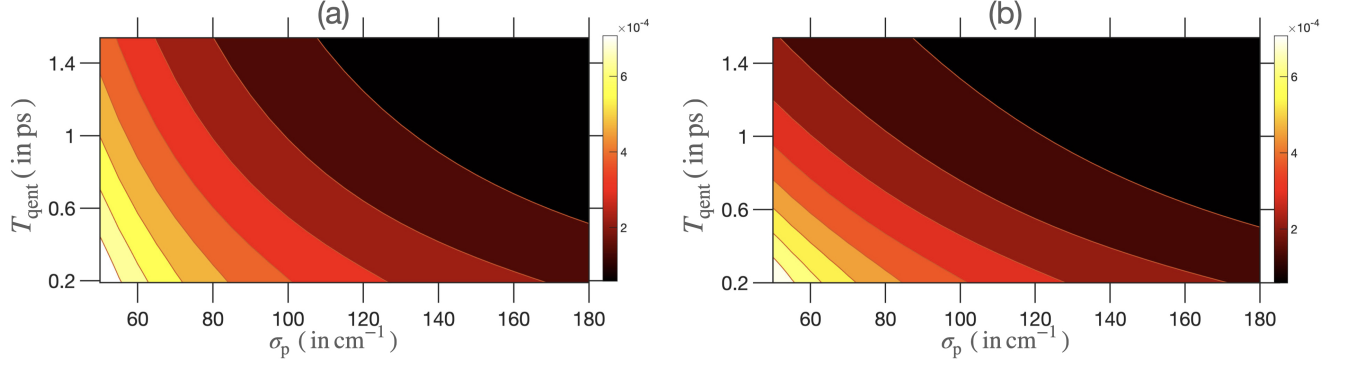


Figure 23. Outgoing entangled beam QFI $\mathcal{Q}(\Gamma; |\Phi_{\text{PDC, out}}\rangle)$, calculated numerically using Eq. (37), for varying entanglement time T_{qent} , and classical pumpwidth σ_p , for TLS parameter Γ and detunings (a) $\Delta = 20$ THz, and (b) $\Delta = 100$ THz. ($\Gamma = 0.15$ THz, $\Gamma_{\perp}/\Gamma = 10.0$.)

Outgoing PDC state QFI for TLS parameter ω_0 for $\Delta \neq 0$ ($\Gamma_{\perp}/\Gamma = 0.5$)

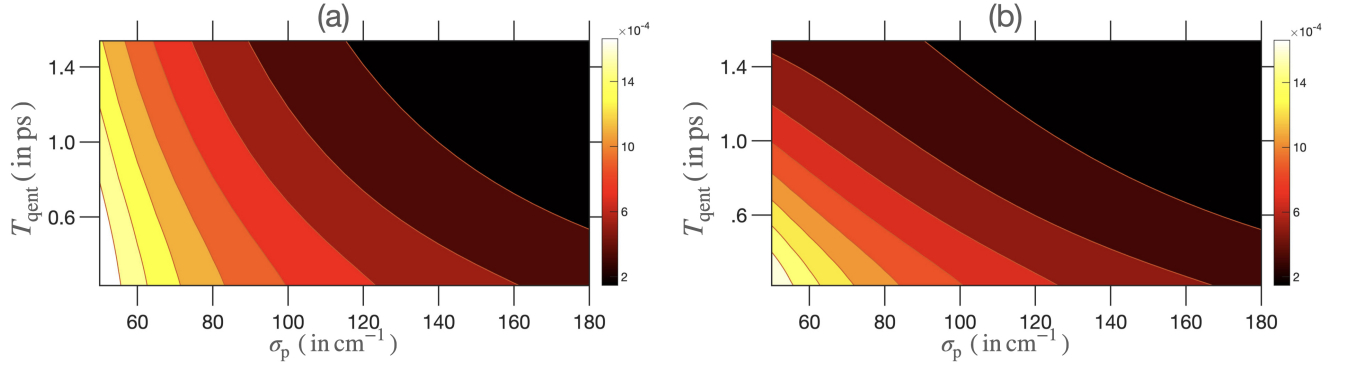


Figure 24. Outgoing entangled beam QFI $\mathcal{Q}(\omega_0; |\Phi_{\text{PDC, out}}\rangle)$, calculated numerically using Eq. (37), for varying entanglement time T_{qent} , and classical pumpwidth σ_p , for TLS parameter ω_0 and detunings (a) $\Delta = 20$ THz, and (b) $\Delta = 100$ THz. ($\Gamma = 0.15$, THz, $\Gamma_{\perp}/\Gamma = 0.5$.)

Outgoing PDC state QFI for TLS parameter ω_0 for $\Delta \neq 0$ ($\Gamma_{\perp}/\Gamma = 10.0$)

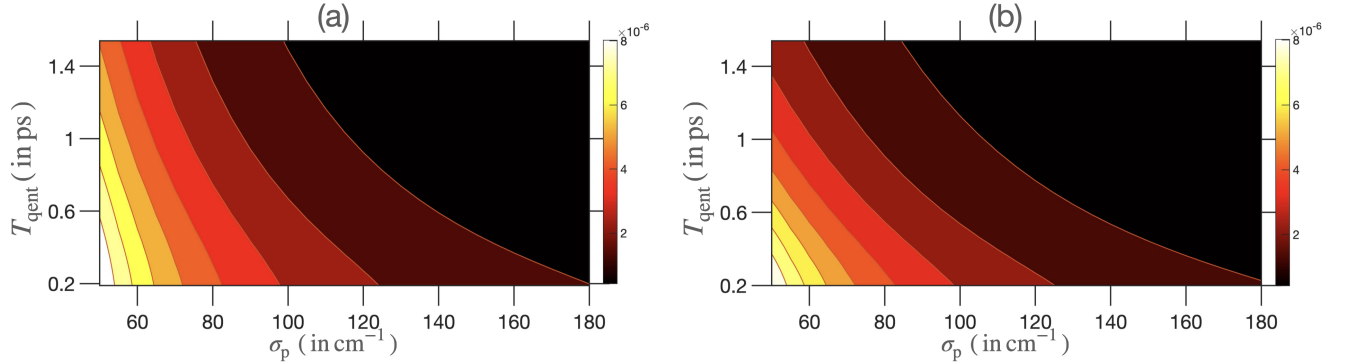


Figure 25. Outgoing entangled beam QFI $\mathcal{Q}(\omega_0; |\Phi_{\text{PDC, out}}\rangle)$, calculated numerically using Eq. (37), for varying entanglement time T_{qent} , and classical pumpwidth σ_p , for TLS parameter ω_0 and detunings (a) $\Delta = 20$ THz, and (b) $\Delta = 100$ THz. ($\Gamma = 0.15$ THz, $\Gamma_{\perp}/\Gamma = 10.0$.)

where J is the coupling strength between the two sites labelled a and b , whose excited levels are respectively $|a\rangle$ and $|b\rangle$, and $|f\rangle$ is the doubly excited state, characterised by level energy $\hbar(\omega_a + \omega_b)$, obtained under the assumption of zero binding energy meaning that there is no interaction between the two excitations.

This Hamiltonian is obtained by setting $P = 2$ in the P -site Hamiltonian in Eq. (11), and is a precursor to the far more complex Frenkel-Holstein Hamiltonians [76–79] that are used to model complex dynamics (including excitonic energy transport (EET) and long-lived quantum beats) in photosynthetic LHCs. In these more involved Hamiltonians, also included are site-dependent reorganisation energy terms, and interaction terms corresponding to phonon baths comprised of harmonic oscillators at each site whose displacement couples linearly with each excitation [77]. This is in addition to modelling each pigment site as a two-level system to account for the lowest transition, as well as interstitial coupling terms that appear in both the n -site and coupled dimer Hamiltonians in Eqs. (11) and (G1) respectively.

For an analytically tractable description of CD dynamics, we transform to the diagonal basis for the CD system, called the excitonic basis, through the eigendecomposition of the Hamiltonian in Eq. (G1),

$$H^{\text{CD}} = \sum_{j=\alpha,\beta} \hbar\omega_j |j\rangle\langle j| + \hbar(\omega_a + \omega_b) |f\rangle \quad (\text{G2})$$

where, effectively, we have diagonalised in the singly-excited manifold (SEM) space only ($|g\rangle$ and $|f\rangle$ states are already eigenstates of H^{CD}), yielding SEM eigenstates $|\alpha\rangle$ and $|\beta\rangle$. The delocalised excitonic states can be explicitly related to the basis kets $|a\rangle$ and $|b\rangle$ by the following relations [80],

$$|\alpha\rangle = \cos \Theta |a\rangle + \sin \Theta |b\rangle, \quad |\beta\rangle = -\sin \Theta |a\rangle + \cos \Theta |b\rangle, \quad (\text{G3})$$

where $\Theta = \frac{1}{2} \arctan(\frac{2J}{\delta})$ and $\delta = \hbar(\omega_a - \omega_b)$, and the corresponding eigenvalues are $\omega_\alpha = \bar{\omega} - (\delta/2) \sec 2\Theta$, $\omega_\beta = \bar{\omega} + (\delta/2) \sec 2\Theta$ respectively for the $|\alpha\rangle$ and $|\beta\rangle$ state. For reference, CD site and excitonic bases are visually represented as level diagrams in Figure 26.

The transition dipole moment operator \mathbf{d} of the CD system that couples with the incoming electric field has the following form in the site basis,

$$\mathbf{d} = \sum_{i=a,b} \boldsymbol{\mu}_{ig} |i\rangle\langle g| + \sum_{i=a,b} \boldsymbol{\mu}_{fi} |f\rangle\langle i| + \text{h.c.} \quad (\text{G4})$$

which we can transform to the excitonic basis using Eq. (G3) where it has the analogous form,

$$\mathbf{d} = \sum_{i=\alpha,\beta} \boldsymbol{\mu}_{ig} |i\rangle\langle g| + \sum_{i=\alpha,\beta} \boldsymbol{\mu}_{fi} |f\rangle\langle i| + \text{h.c.} \quad (\text{G5})$$

such that the various vector dipole elements transform via the following Θ -rotation matrix,

$$\begin{aligned} \begin{bmatrix} \boldsymbol{\mu}_{\alpha g} \\ \boldsymbol{\mu}_{\beta g} \end{bmatrix} &= \begin{bmatrix} \cos \Theta & \sin \Theta \\ -\sin \Theta & \cos \Theta \end{bmatrix} \begin{bmatrix} \boldsymbol{\mu}_{ag} \\ \boldsymbol{\mu}_{bg} \end{bmatrix}, \\ \begin{bmatrix} \boldsymbol{\mu}_{f\alpha} \\ \boldsymbol{\mu}_{f\beta} \end{bmatrix} &= \begin{bmatrix} -\sin \Theta & \cos \Theta \\ \cos \Theta & \sin \Theta \end{bmatrix} \begin{bmatrix} \boldsymbol{\mu}_{fa} \\ \boldsymbol{\mu}_{fb} \end{bmatrix}. \end{aligned} \quad (\text{G6})$$

As we will restrict our discussion to the use of pulses carrying single excitation to the CD system, and the CD system itself being in the ground state $|g\rangle$ at $t = 0$, the dipole operator elements $\boldsymbol{\mu}_{fi}$ that link the SEM and doubly excited level $|f\rangle$ can be dropped altogether. We will then abbreviate the GSM-SEM transition dipoles for brevity as $\boldsymbol{\mu}_{ig} \equiv \boldsymbol{\mu}_i = |\boldsymbol{\mu}_i| \hat{\boldsymbol{\mu}}_i$, $i = \alpha, \beta$ for brevity.

In order to describe the light-CD interaction, we transform to the interaction picture with respect to the zeroth-order Hamiltonian,

$$H_0^{\text{CD}} = \sum_{i=\alpha,\beta} \hbar\bar{\omega}_S |i\rangle\langle i| + 2\hbar\bar{\omega}_S |f\rangle\langle f| + H^{\text{F}}, \quad (\text{G7})$$

where $\bar{\omega}_S$ is the central frequency of the signal mode, and the free field Hamiltonian is

$$H^{\text{F}} = \int d\omega \hbar\omega a_S^\dagger(\omega) a_S(\omega) + \int d\omega \hbar\omega b^\dagger(\omega) b(\omega), \quad (\text{G8})$$

where we have dropped the free field term corresponding to idler mode because of the explicit assumption that the CD system only interacts with a single mode in this input-output setup, and the operator $b(t)$ corresponds to the

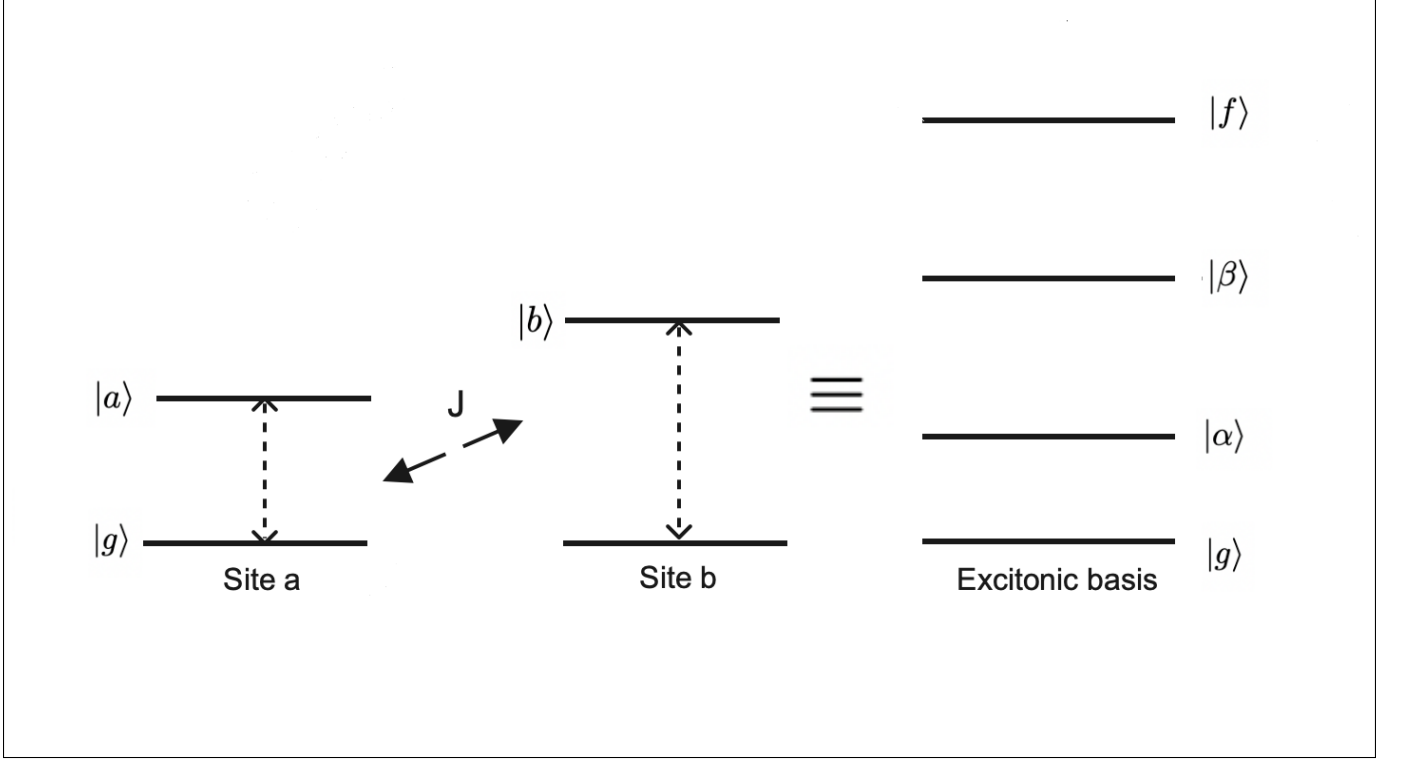


Figure 26. Level diagram of the CD system comprised of two two-level systems that have a common ground set to zero energy, and excited levels $|a\rangle$ and $|b\rangle$, coupled to each other via Coulomb interaction of strength J . In the diagonal excitonic basis effectively in the SEM space, $|\alpha\rangle$ and $|\beta\rangle$ are delocalised over both sites a and b.

environmental modes E. The interaction picture Hamiltonian is then

$$\begin{aligned} H^{\text{CD}}(t) &= H_I^{\text{CD}} - \mathbf{d} \cdot \mathbf{E}(t) \\ &= \sum_{i=\alpha,\beta} \hbar \Delta_i |i\rangle \langle i| + \hbar(\Delta_\alpha + \Delta_\beta) |f\rangle \langle f| - i\hbar [\sqrt{\Gamma} \Sigma^\dagger a_S(t) \otimes \mathbf{1}^I \otimes \mathbf{1}^E + \sqrt{\Gamma_\perp} \Sigma^\dagger \mathbf{1}^S \otimes \mathbf{1}^I \otimes b(t) - \text{h.c.}] \end{aligned} \quad (\text{G9})$$

where

$$\begin{aligned} \Sigma^\dagger &= \sqrt{\frac{\omega_c \mu_0^2}{2\epsilon_0 c A_0 \hbar}} (\lambda_\alpha \sigma_+^\alpha + \lambda_\beta \sigma_+^\beta) \\ &= \sqrt{2\Gamma} (\lambda_\alpha \sigma_+^\alpha + \lambda_\beta \sigma_+^\beta), \text{ where } \sigma_+^i = |i\rangle \langle g|, \lambda_i = (\hat{\epsilon} \cdot \hat{\mu}_i) \left(\frac{|\mu_i|}{\mu_0} \right) \quad (i = \alpha, \beta) \end{aligned} \quad (\text{G10})$$

is the collective SEM raising operator, and

$$H_I^{\text{CD}} = \sum_{i=\alpha,\beta} \hbar \Delta_i |i\rangle \langle i| + \hbar(\Delta_\alpha + \Delta_\beta) |f\rangle \langle f| \quad (\text{G11})$$

where $\Delta_i = \omega_i - \bar{\omega}_S$ ($i = \alpha, \beta$) are the detunings from the central signal pulse frequency of the excitonic levels, and $a(t)$ are white-noise operators previously defined in Eq (14) corresponding to the incoming paraxial mode. In obtaining these, we have re-centered the frequency integrals with the transformation $\omega \rightarrow \omega - \bar{\omega}_S$ so that the field operators $a_S(\omega)$ and $b(\omega)$ are centred around $\omega = 0$. The extension of the frequency integrals to all frequencies from $-\infty$ to $+\infty$ is a consequence of the fact that the CD system-quantum pulse interaction is assumed to be peaked around the central frequency of the oncoming pulse, allowing us to invoke the white noise approximation of SVEA.

Appendix H: Characteristic Matter Function For Bare CD Hamiltonian

Closed expressions for the characteristic function $f^{\text{CD}}(t_1)$ can be calculated explicitly for the bare CD Hamiltonian using the following formula for matrix exponential of a 2×2 matrix $M = \begin{pmatrix} a & b \\ c & d \end{pmatrix} \in \mathbf{C}^{2 \times 2}$ [81]

$$e^M = e^{\frac{a+d}{2}} \begin{pmatrix} \cosh v + \frac{a-d}{2} \frac{\sinh v}{v} & b \frac{\sinh v}{v} \\ c \frac{\sinh v}{v} & \cosh v - \frac{a-d}{2} \frac{\sinh v}{v} \end{pmatrix}. \quad (\text{H1})$$

where $v = (1/2)\sqrt{(a-d)^2 + 4bc}$.

For the bare CD Hamiltonian, the characteristic function can be expressed as the expectation value of the matrix exponential

$$f_{\text{CD}}(t_1) = (\lambda_\alpha \ \lambda_\beta) \exp \left[-\frac{iH_I^{\text{CD}} t_1}{\hbar} - \frac{1}{2} \Sigma^\dagger \Sigma t_1 \right] \begin{pmatrix} \lambda_\alpha \\ \lambda_\beta \end{pmatrix} \quad (\text{H2})$$

which is then

$$f_{\text{CD}}(t_1) = e^{-i\tilde{\Delta}t_1 - \frac{\Gamma t_1}{2}(\lambda_\alpha^2 + \lambda_\beta^2)} \left\{ (\lambda_\alpha^2 + \lambda_\beta^2) \cosh v + \frac{\sinh v}{v} \left[(\lambda_\alpha^2 - \lambda_\beta^2) \frac{a-d}{2} - 2\lambda_\alpha^2 \lambda_\beta^2 \Gamma t_1 \right] \right\} \quad (\text{H3})$$

where $\tilde{\Delta} = (\Delta_\alpha + \Delta_\beta)/2$ is the averaged detuning, and the various terms (in terms of the CD parameters) are

$$v = \frac{t_1}{2} \sqrt{\frac{-\delta^2 \sec^2 2\Theta}{\hbar^2} + \Gamma^2 (\lambda_\alpha^2 + \lambda_\beta^2)^2 - \frac{2i\delta\Gamma}{\hbar} \sec 2\Theta (\lambda_\alpha^2 - \lambda_\beta^2)} \quad (\text{H4})$$

and

$$\frac{a-d}{2} = \frac{i\delta t_1 \sec 2\Theta}{2\hbar} - \frac{\Gamma t_1}{2} (\lambda_\alpha^2 - \lambda_\beta^2). \quad (\text{H5})$$

The QFI for the outgoing single photon state that scatters off of the CD system is proportional to a convolution of the incoming field envelope, and the parametric derivative of the characteristic function $f_{\text{CD}}(t_1)$ which can also be calculated explicitly for the bare CD Hamiltonian for the J parameter,

$$\begin{aligned} \frac{\partial}{\partial J} f_{\text{CD}}(t_1) &= e^{-i\tilde{\Delta}t_1 - \frac{\Gamma t_1}{2}(\lambda_\alpha^2 + \lambda_\beta^2)} \left[\frac{\partial v}{\partial J} \left\{ (\lambda_\alpha^2 + \lambda_\beta^2) \sinh v + \left(\frac{\cosh v}{v} - \frac{\sinh v}{v^2} \right) \left((\lambda_\alpha^2 - \lambda_\beta^2) \frac{a-d}{2} - 2\lambda_\alpha^2 \lambda_\beta^2 \Gamma t_1 \right) \right\} \right. \\ &\quad \left. + \frac{\delta}{\delta^2 + 4J^2} \frac{\sinh v}{v} \left\{ 4\lambda_\alpha \lambda_\beta \frac{a-d}{2} + (\lambda_\alpha^2 - \lambda_\beta^2) \frac{i\delta t_1}{\hbar} \sec 2\Theta \tan 2\Theta + 2\Gamma t_1 \lambda_\alpha \lambda_\beta (\lambda_\alpha^2 - \lambda_\beta^2) \right\} \right] \quad (\text{H6}) \end{aligned}$$

where

$$\frac{\partial v}{\partial J} = \frac{\delta}{\delta^2 + 4J^2} \frac{t_1}{8v} \left\{ -\frac{4\delta^2}{\hbar^2} \sec^2 2\Theta \tan 2\Theta - \frac{4i\delta\Gamma}{\hbar} \sec 2\Theta \tan 2\Theta (\lambda_\alpha^2 - \lambda_\beta^2) - \frac{8i\delta\Gamma}{\hbar} \sec 2\Theta \lambda_\alpha \lambda_\beta \right\}. \quad (\text{H7})$$

Appendix I: Relation Between QFI of PDC State and Post-Selected Biphoton State

The vacuum term in the two-photon PDC state in Eq. (56) does not contribute to the detected signal, and is often dropped in theoretical analyses by post-selecting for the detected two-photon states only. The post-selected biphoton state, renormalised to ensure a unit norm, can be expressed in terms of the PDC JTA as:

$$|\Phi_{\text{biph}}\rangle = \frac{1}{\sqrt{\Lambda}} \int dt_S \int dt_I \Phi_{\text{PDC}}(t_S, t_I) a_S^\dagger(t_S) a_I^\dagger(t_I) |0\rangle \quad (\text{I1})$$

where $\Lambda = \int dt_S \int dt_I \Phi_{\text{PDC}}^*(t_S, t_I) \Phi_{\text{PDC}}(t_S, t_I)$ is the normalisation factor for the post-selected state. We can then work out the outgoing state corresponding to the biphoton state in Eq. (I1) for arbitrary matter systems with Hamiltonian H_I^M , also in terms of the PDC JTA:

$$|\Phi_{\text{biph, out}}\rangle = \frac{1}{\sqrt{\Lambda}} \int dt_S \int dt_I \Phi_{\text{PDC, out}}(t_S, t_I) a_S^\dagger(t_S) a_I^\dagger(t_I) |0\rangle \quad (\text{I2})$$

where $\Phi_{\text{PDC,out}}(t_S, t_I) = \sum_n r_{n,\text{PDC}} \phi_{n,\text{PDC}}^S(t_S) h_n^I(t_I)$. This can then be used to calculate the corresponding QFI for parameter θ ,

$$\mathcal{Q}(\theta; |\Phi_{\text{biph,out}}\rangle) = \frac{4}{\Lambda} \left[\int dt_S \int dt_I \frac{\partial \Phi_{\text{PDC,out}}(t_S, t_I)^*}{\partial \theta} \frac{\partial \Phi_{\text{PDC,out}}(t_S, t_I)}{\partial \theta} - \frac{1}{\Lambda} \left| \int dt_S \int dt_I \frac{\partial \Phi_{\text{PDC,out}}(t_S, t_I)^*}{\partial \theta} \Phi_{\text{PDC,out}}(t_S, t_I) \right|^2 \right]. \quad (\text{I3})$$

The outgoing PDC state QFI and the post-selected state QFI are then related to each other as

$$\mathcal{Q}(\theta; |\Phi_{\text{biph,out}}\rangle) = \frac{N_{\text{PDC}}}{\Lambda} \mathcal{Q}(\theta; |\Phi_{\text{PDC,out}}\rangle) + \frac{4(\Lambda - 1)}{\Lambda^2} \left| \int dt_S \int dt_I \frac{\partial \Phi_{\text{PDC,out}}(t_S, t_I)^*}{\partial \theta} \Phi_{\text{PDC,out}}(t_S, t_I) \right|^2. \quad (\text{I4})$$

It is interesting to note the contrasting nontriviality of this relation (where the transformation between the two QFIs depends on the value of the true value of the parameter θ) vis-à-vis the transformation of the QFI function when the parameter is rescaled (in which case the QFI is rescaled by the square of the constant scaling factor $\mathcal{Q}(\theta/c; |\psi\rangle\langle\psi|) = (1/c^2)\mathcal{Q}(\theta; |\psi\rangle\langle\psi|)$).

The biphoton normalisation factor Λ is proportional to the rate of entangled photon production given by $(\alpha_{\text{pump}}^2/\hbar^2)$, which is typically a very small number given that the PDC process only converts between one in 10^6 to 10^{11} pump photons into entangled daughter photons, depending on the particular nonlinear crystal used, and other experimental variables. In this text, for our choice of $\alpha_{\text{pump}}/\hbar = 0.01$, we can safely conclude that $\Lambda \ll 1$, and (by the same token) $N_{\text{PDC}} \approx 1$. This yields the simpler relation between the two QFIs,

$$\mathcal{Q}(\theta; |\Phi_{\text{PDC,out}}\rangle) \approx \frac{\Lambda}{N_{\text{PDC}}} \mathcal{Q}(\theta; |\Phi_{\text{biph,out}}\rangle) + \frac{4}{\Lambda N_{\text{PDC}}} \left| \int dt_S \int dt_I \frac{\partial \Phi_{\text{PDC,out}}(t_S, t_I)^*}{\partial \theta} \Phi_{\text{PDC,out}}(t_S, t_I) \right|^2. \quad (\text{I5})$$